

# Optical and Near-infrared View of Planet-forming Disks and Protoplanets

**Myriam Benisty**

*Univ. Grenoble Alpes, CNRS, IPAG, 38000 Grenoble, France*

**Carsten Dominik**

*Anton Pannekoek Institute for Astronomy, University of Amsterdam, Science Park 904, 1098 XH Amsterdam, The Netherlands*

**Katherine Follette**

*Physics & Astronomy Department, Amherst College, 21 Merrill Science Dr., Amherst, MA 01002*

**Antonio Garufi**

*INAF, Osservatorio Astrofisico di Arcetri, Largo Enrico Fermi 5, I-50125 Firenze, Italy*

**Christian Ginski**

*Anton Pannekoek Institute for Astronomy, University of Amsterdam, Science Park 904, 1098 XH Amsterdam, The Netherlands*

**Jun Hashimoto**

*Astrobiology Center, National Institutes of Natural Sciences, 2-21-1 Osawa, Mitaka, Tokyo 181-8588, Japan*

**Miriam Keppler**

*Max Planck Institute for Astronomy, Königstuhl 17, 69117, Heidelberg, Germany*

**Willy Kley**

*Institut für Astronomie und Astrophysik, Universität Tübingen, Auf der Morgenstelle 10, 72076 Tübingen, Germany*

**John Monnier**

*Astronomy Department, University of Michigan, Ann Arbor, MI 48109, USA*

In this chapter, we review the breakthrough progress that has been made in the field of *high-resolution, high-contrast optical and near-infrared* imaging of planet-forming disks. These advancements include the *direct detection* of protoplanets embedded in some disks, and *derived limits* on planetary masses in others. Morphological substructures, including: rings, spirals, arcs, and shadows, are seen in all imaged infrared-bright disks to date, and are ubiquitous across spectral types. These substructures are believed to be the result of disk evolution processes, and in particular disk-planet interactions. Since small dust grains that scatter light are tightly bound to the disk's gas, these observations closely trace disk structures predicted by hydrodynamical models and serve as observational tests of the predictions of planet formation theories. We argue that the results of current and next-generation high-contrast imaging surveys will, when combined with complementary data from ALMA, lead to a much deeper understanding of the co-evolution of disks and planets, and the mechanisms by which planets form.

## **In memory of Prof. Willy Kley**

*We dedicate this chapter to our co-author Willy Kley, who unexpectedly passed away in December 2021. His unique contributions to our field, and his optimism and kindness will be remembered for a long time. An obituary written by Richard Nelson can be found at the end of this Chapter.*

## **1. Introduction**

### **1.1. Motivation**

Transit, radial velocity, and imaging surveys have discovered and confirmed over 4500 exoplanets<sup>1</sup> indicating that planet formation is a robust and efficient process. Ob-

<sup>1</sup>September 2021; <https://exoplanets.nasa.gov/discovery/exoplanet-catalog/>

serving campaigns have also confirmed that planetary systems show an incredible diversity in the nature of individual planets and in the architecture of planetary systems. Confirmed planetary systems span a range of star-planet separations and masses, from widely-separated Super-Jupiters at tens to hundreds of astronomical units (au) (e.g. *Marois et al.* 2008) to compact Super-Earth systems compressed to within just a few au from their host stars (e.g. *Lissauer et al.* 2011). Planet formation has also been confirmed to occur in multiple star systems, where around a dozen planets have been found (*Kostov et al.* 2016). The origin of this extreme diversity, and whether it is inherited from the earliest stages of planet formation in protoplanetary disks, is unknown. Since protoplanetary disks set the initial conditions for planet formation, the observed diversity of exoplanets might well be related to the diversity of disk physical properties. The evolution of bulk disk gas and dust will be key in determining where, when, and how planets form and evolve. The interaction of planets with their host disk is another key piece of the puzzle in planetary evolution; massive planets form first and can dramatically affect disk structure (*Bae et al.* 2018), influencing the formation and evolution of lower-mass planets, and dominating the dynamical evolution of the planet-star-disk system (see Chapters *Bae et al.*; *Paardekooper et al.*).

To understand the diverse outcomes of planet formation, it is therefore crucial to understand the structure of protoplanetary disks from the epoch of formation and throughout the disk evolutionary sequence, using the disks' morphological appearances as essential clues. Planet formation and disk evolution processes occur simultaneously, influence one another, and jointly shape disk structures. The two main imprints of these processes on the disk are (i) perturbations in the disk structure (that is, formation of substructures), and (ii) spatial differentiation of gas and dust. High-resolution imaging of gas and dust grains in protoplanetary disks affords a direct probe of both imprints. To probe disk evolution, large samples of high-resolution multiwavelength disk imagery across a wide range of disk evolutionary stages are required.

Until recently, disk observations were limited in angular resolution and could not provide clear constraints on the physical processes driving their evolution. Modeling spectral energy distributions (SEDs) derived from whole-disk photometry cannot unambiguously determine the disk structure, as it is highly degenerate (*Woitke et al.* 2019). In the past few years, major progress in instrumentation has enabled some limitations to be overcome and has dramatically affected both observational and theoretical studies of planet formation. The advent of the Atacama Large Millimeter/sub-millimeter Array (ALMA) allowed us to spatially resolve the thermal emission of cold, large (mm-sized) dust grains and molecules in circumstellar disks (e.g., *Dutrey et al.* 2014) and circumplanetary disks (CPDs) (*Isella et al.* 2019; *Benisty et al.* 2021). In the optical and near-infrared (near-IR) regime, telescopes with extreme adaptive optics (AO) enabled nearly diffraction-

limited imaging ( $\sim 4$  au at 100 pc), providing access to both thermal emission from young planets and dust in CPDs, as well as to the scattered light from small (micron-sized) dust grains in the disk surface layers (*Keppler et al.* 2018). The first images of disks obtained at high resolution revealed a greater complexity than previously envisioned (*Quanz et al.* 2011; *ALMA Partnership et al.* 2015), revolutionizing our view of protoplanetary disk evolution. The first surveys with ALMA and high-contrast near-IR imagers suggested that small-scale substructures are frequent and have a variety of morphologies, locations, and properties (*Andrews 2020*; *Garufi et al.* 2018). The direct comparison of images obtained at different wavelengths allows us to constrain the radial and vertical distributions of gas and dust in disks. Indeed, large grains settle to the midplane, and small grains are well coupled to the gas, covering the full vertical gas extent of the disk. Therefore, multi-wavelength observations trace different disk layers (e.g., *Dong et al.* 2012a) and enable construction of a three-dimensional view of the disk physical conditions.

One of the major quests in our field is to identify and constrain favorable conditions for planet formation. We need to know where, when, and how planets form, and whether there are significant differences in the planet population as a function of system age and location in the disk. In the core-accretion model (*Pollack et al.* 1996), planet formation starts with the growth of dust grains to planetesimal sizes. However, pressure gradients in the gas will lead to sub- or sometimes super-Keplerian velocities of the gas. Dust grains then feel a drag force that causes them to drift radially towards regions of the disk with higher pressure, usually toward the inner disk. In the absence of a way to reduce or stop radial drift, this effect results in all dust grain orbits decaying toward the star before any planet could form (*Weidenschilling 1977*). Local variations of the gas pressure (reversing the radial pressure gradient) provide a way to maintain these dust grains in the disk, as dust grains with Stokes number close to 1 (*Birnstiel et al.* 2010) will move to the nearby local pressure maximum and get trapped there (e.g., *Pinilla et al.* 2012). In these so-called dust traps, grains can grow efficiently to pebble sizes, and when a high dust to gas ratio is reached, streaming instabilities can occur and lead to the formation of planetesimals (*Youdin and Goodman 2005*). These local variations of the gas pressure will lead to distinct observable features (substructures) at different tracers (gas lines, scattered light and thermal emission images) (e.g., *Baruteau et al.* 2019). The typical size gas substructures is the pressure scale height, which is about one to several au at separations of few tens of au from the central star, a scale accessible with high angular resolution observations.

Generally speaking, observed disk substructures can thus be both the *cause* (as favored locations of planetesimal growth), and the *consequence* (as imprints of massive forming planets) of planets in disks. Therefore, theoretical studies aimed at constraining the origin of substructures are pivotal (see Chapters *Bae et al.*; *Lesur et al.*; *Paardekooper*

*et al.*). In short, substructures can be created by the dynamical evolution of the gas in the disk, through (magneto-)hydrodynamical instabilities and disk winds (e.g., *Riols et al.* 2020a). Such processes lead to both symmetric and asymmetric pressure perturbations, which will in turn trap dust grains. On the other hand, substructures may be signposts of embedded, yet-undetected, protoplanets. For example, planets launch spiral density waves at Lindblad resonances, deplete their orbit of material (*Kley et al.* 2001) leading to dust and gas depleted gaps (*Bae et al.* 2017), or even large cavities. The characteristics of these gaps and cavities depend on the planet mass and orbital parameters and on the disk viscosity. Planet-disk interactions also often trigger large-scale hydrodynamical instabilities (vortices; *Meheut et al.* 2010) that lead to strong azimuthal asymmetries. Disk substructures can therefore serve as a guide to detect hidden planets (*Dong et al.* 2019) as well as a local probe of the disk conditions while dynamical interactions are ongoing. An extensive study of the prevalence and properties of substructures will allow us to determine the relative importance of the various mechanisms driving disk evolution, and can help constraining a yet-undetected population of exoplanets that can then be compared to the demographics of more evolved exoplanetary systems (see Chapter *Bae et al.*).

Early results from scattered light disk imaging were previously discussed in the Protostars & Planets (PP) series (PPV; *Watson et al.* 2007 and PPVI; *Espaillet et al.* 2014), and are summarized in the following paragraph. Hubble Space Telescope images provided the first evidence of substructures in disks, in particular around Herbig AeBe stars which presented extended nebulosity (*Grady et al.* 1999; *Fukagawa et al.* 2004). Spiral features were detected around HD100546 (*Pantín et al.* 2000; *Grady et al.* 2001) and HD141569A (*Mouillet et al.* 2001; *Clampin et al.* 2003), and radial clearing and fading of the outer disk were observed in HD141569A and TW Hya respectively (*Weinberger et al.* 1999; *Krist et al.* 2000). Observations of the silhouette of edge-on disks enabled determination of disk scale heights (e.g., *Perrin et al.* 2006), supported by model fitting (*Watson et al.* 2004). Detailed analysis of multi-wavelength images of GG Tau provided evidence for dust stratification in the disk from the scattering phase function (*McCabe et al.* 2002; *Duchêne et al.* 2004). Between PPV and PPVI, near-IR polarimetric disk observations were conducted, in particular through the SEEDS (Strategic Explorations of Exoplanets and Disks with Subaru) survey (e.g., *Thalmann et al.* 2010; *Hashimoto et al.* 2012; *Mayama et al.* 2012; *Takami et al.* 2013), and VLT/NACO observations (e.g., *Quanz et al.* 2011, 2012) providing further support for the presence of substructures (cavities, rings, spirals) in IR-bright disks. The focus of the *Espaillet et al.* (2014) PPVI review was on transition disks (there referred to as transitional, and pre-transitional disks).

Since PPVI, monumental progress has been achieved in the field of high-resolution disk imaging, indicating the ubiquity of substructures in scattered light. Another major

result since PPVI, is the first and so far unique discovery of a protoplanetary system still embedded in its birth environment, PDS 70. This chapter is a review of major results in the field of optical and near-IR high-resolution disk imaging, as well as highlights of relevant results from other, highly complementary, observational techniques. Large emphasis is placed on the disk substructures resolved by polarimetric images from ground-based telescopes since much of the recent work of the community has been in this area. Figure 1 is a compilation of such images, highlighting a number of the results reviewed in this chapter. The data presented in the figure presents the pinnacle of our current observational capabilities in the optical and near-IR direct imaging of circumstellar disks, achieved thanks to leading observational facilities such as the Subaru telescope, the Gemini-South telescope, and the ESO Very Large Telescope. The methodology and instruments used are described in Section 2 of the chapter. Section 3 provides a general theoretical background for understanding substructures, Section 4 reviews results on the global structure of disks and the properties of dust grains, and Section 5 presents an overview of observations of disk substructures, such as cavities, rings, spiral arms, and shadows. In Section 6, we discuss the discovery of the first young embedded planetary system along with a review of current upper limits for other systems. We discuss future avenues for research in the field of direct imaging of disks and protoplanets in Section 7, and summarize our chapter in Section 8.

## 2. Methodology

At optical and near-IR wavelengths, the star itself and the hot innermost disk regions are the primary sources of photons. While the current generation of single-dish telescopes cannot spatially resolve thermal emission from the disk regions inwards of a few au, thermal emission from planets located at separations larger than 10 au are, in principle, observable if these planets are not heavily embedded. At similar separations, 10s of au from the star, the protoplanetary disk can be mapped in scattered light. Small (sub-) $\mu\text{m}$ -sized dust grains and aggregates, which are well coupled to the gas, can efficiently scatter stellar photons at optical and near-IR wavelengths. The gas- and dust-rich planet-forming disks depicted in Figure 1 are optically thick to optical and near-IR radiation (*Chiang and Goldreich* 1997). Scattered light observations will therefore be sensitive to the optical depth  $\tau \sim 1$  layer located in the surface of the disk. As such, it will be directly related to both the stellar irradiation (that drops off radially with the squared distance to the star) and the local inhomogeneities in the surface. Therefore, the net amount of observed scattered photons depends on both the number of photons incident on the disk surface and the availability of scattering dust grains.

### 2.1. Requirements

High-contrast imaging of planet-forming disks in the optical and near-IR faces several challenges, namely the need

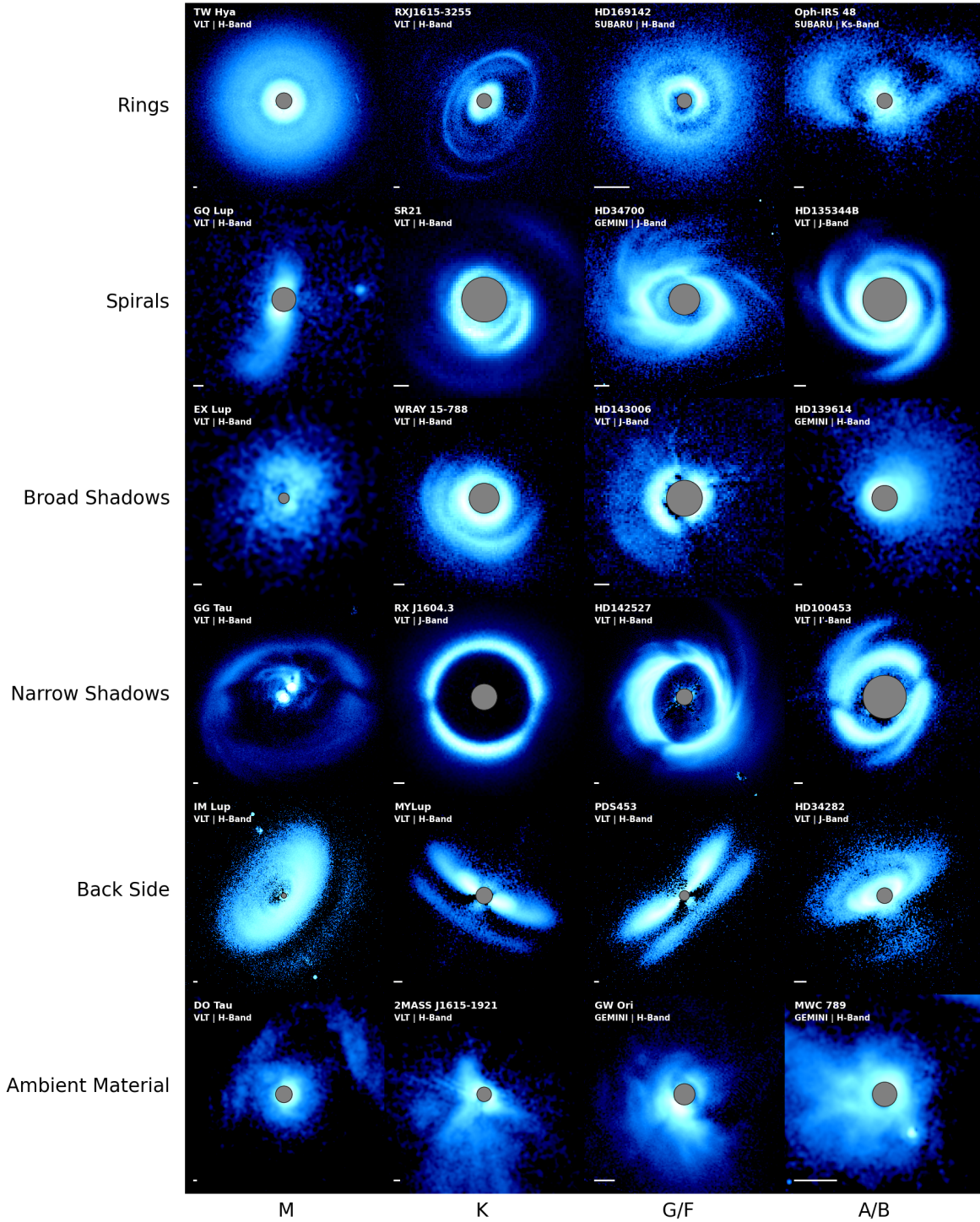


Fig. 1.— Gallery of disks observed with the SPHERE, GPI, and HiCIAO instruments, highlighting the wide range of morphological features present in planet-forming disks and their ubiquity across spectral types. All images are normalized within the depicted stamp and colorbars are arcsinh scaled. A 50 au scalebar appears in the lower left corner of each image, and grey central circles mark regions obscured by a coronagraph. North is up and East to the left in all images. The star name, instrument, and wavelength are indicated in the upper left corner of each image. In all cases, the polarimetric  $Q_\phi$  image is shown, with the exception of GG Tau, for which we show polarized intensity. Images are coarsely sorted by spectral type (x axis) and morphological type (y axis), though we note that many disks exhibit features matching multiple morphological categories. All relevant references for individual systems are listed in appendix A. Figures 8, 9 and 10 provide additional disk images.



for high angular resolution and high contrast, as well as cancellation of atmospheric perturbations if observations are obtained with ground-based instruments. The structures that we aim to observe have typical widths of the pressure scale height  $H$  in the gas (Dullemond *et al.* 2018), which depends on the local sound speed and on the Keplerian angular velocity. For typical disk models,  $H/R$  is typically 0.05-0.1 at radii of tens of au, implying that substructures have typical widths of a few au at most. This requires the use of large diameter telescope facilities. Indeed, nearby reservoirs of young stellar objects in low-mass star forming regions (e.g., the Taurus and Lupus molecular cloud complexes, or the Chamaeleon I cloud) are located at distances between  $\sim 150$  pc and 200 pc (Dzib *et al.* 2018; Luhman 2018). At such distances, 6-8 au translates into on-sky angular scales of  $\sim 0.040''$ , for a diffraction limited resolution element on an 8m-class telescope in the H-band ( $\lambda = 1.65 \mu\text{m}$ ). This also means that, with the largest currently available telescope facilities (8-10 m telescopes such as the Very Large Telescope, Subaru, and Gemini), only the disk regions beyond a few au can be spatially resolved. The angular resolution that is actually achieved by the current observations depends on the wavelength regime and, in the showcase examples of Figure 1, ranges from 25 mas to 70 mas. Therefore, for objects in Taurus and Lupus (e.g., GG Tau and IM Lup), this translates to scales of 4 to 10 au. In the more distant star forming region of Orion (e.g. GW Ori), we are still able to resolve scales between 10 and 30 au. To give an impression of the different extents of the systems and of the observed sub-structures, each image in Figure 1 is accompanied by a scale bar of 50 au in the lower left corner.

To reach the theoretical diffraction limit with a large ground-based telescope, the disrupting effect of the atmosphere needs to be compensated for. This requires the employment of active or adaptive optics systems (Babcock 1953). This technology in particular has seen crucial advancements in the past decade, leading to the latest generation of so called "extreme" AO systems (Fusco *et al.* 2006; Macintosh *et al.* 2006; Jovanovic *et al.* 2015; Guyon 2018). Nowadays, images of planet-forming disks are routinely obtained at wavelengths ranging from I-band ( $\sim 0.8 \mu\text{m}$ ) to K-band ( $\sim 2.2 \mu\text{m}$ ), as is clear from Figure 1. The observations at different wavelengths were initially driven by technical considerations. K-band and H-band observations are generally favored due to the increase stability of the atmosphere at longer wavelengths. Optical observations deliver superior angular resolution, but can only be conducted for very bright target stars due to adaptive optics requirements.

Another requirement is the need to achieve high contrast between the primary star and the scattered light from circumstellar dust in the disk, as scattered light from the disk is significantly fainter than the star. For gas-rich flared disks, the observed average contrast between the polarized and stellar flux is on the order of  $10^{-2}$  to  $10^{-4}$  (Garufi *et al.* 2018, see Sect. 4.1). Blocking star light first requires the use of a coronagraphic mask, but is generally optimized

by combining coronagraphic hardware design with advanced observational and post-processing techniques, as discussed below. The scientific progress in the field has been enabled by significant advancements in all three areas.

## 2.2. Differential imaging techniques

Even with the use of AO and state-of-the-art coronagraphs, additional image post-processing is needed to disentangle the stellar speckle halo from scattered light originating in the circumstellar environment. For this purpose, differential imaging techniques are used, combining optimal observational strategies and data reduction techniques.

### 2.2.1. Reference Differential Imaging.

The most straightforward technique is reference differential imaging (RDI). It relies on observations of a reference star with similar spectral properties and apparent magnitude to the scientific target, which are used to calibrate the instrument point spread function (PSF). In an idealized scenario, the instrument and sky conditions remain identical between the two observations, and thus the PSF will not change. One can then use the reference star image to subtract the stellar light from the science target image, leaving only the disk or planet signal. This technique has the great advantage that it in principle does not reduce the throughput of the scientifically interesting signal from circumstellar disks and planets. In practice, it has been mainly used in space-based observations (Grady *et al.* 1999; Weinberger *et al.* 1999; Grady *et al.* 2000, 2001; Debes *et al.* 2017; Choquet *et al.* 2016), as the PSF stability is superior relative to ground-based observations. Libraries of reference stars can be constructed using all existing observations in the same instrument mode. This strategy, pioneered for the Hubble Space Telescope, was applied to HST/NICMOS data in the Archival Legacy Investigations of Circumstellar Environments (ALICE, Choquet *et al.* 2014). In addition to choosing the optimal reference star, principal component analysis (PCA) based reduction algorithms are used to deconstruct the reference star images and fit them to the science star. When a bright circumstellar disk is present, this can result in over-fitting the data images. In practice, this over-fitting significantly limits the throughput of circumstellar signal, especially for disks that appear bright in scattered light. Over-fitting can be counteracted by iterative approaches that disentangle disk and stellar signal. One recent advancement was made by Ren *et al.* (2018), who use non-negative matrix factorization for this purpose. With the advent of extreme AO systems leading to better correction of the atmospheric perturbations, RDI is now maturing as a differential imaging technique (Boccaletti *et al.* 2021). Recently, Wahhaj *et al.* (2021) presented results obtained with VLT/SPHERE on the HR8799 system, obtaining a point-source contrast limit of 11.2 magnitudes at  $0.1''$ , through alternated observations of science target and reference star. This strategy is now increasingly used

in ongoing programs. However, finding the optimal reference star can be difficult, especially in regions of the sky offset from the galactic plane where the stellar density is lower. Since changing atmospheric conditions usually limit the contrast achieved with RDI from the ground, other techniques rely on the science data itself to disentangle stellar and circumstellar light.

### 2.2.2. Angular Differential Imaging.

The most widely used technique is angular differential imaging (ADI). ADI was originally designed for the detection of faint thermal emission from wide-separation extrasolar planets (Marois et al. 2006). The ADI technique uses the apparent rotation of the stellar field on the sky during a night, when observed with an altitude-azimuth mounted telescope. Instruments on such telescopes usually have a K-mirror build in, the so-called "de-rotator", to field-stabilize the image of the sky on the detector. For ADI observations, field-stabilization is switched off, and instead all optical components relative to the telescope entrance pupil are stabilized. In this so-called "pupil-stabilized" mode, one attempts to keep the instrumental PSF and the unresolved stellar image stable, while off-axis stars, planets or disk signal will show apparent rotation, enabling to clearly identify those. This technique in a simpler form was pioneered with the Hubble Space Telescope ("roll-subtraction") where the entire telescope was rolled around the optical axis between exposures (Schneider and Silverstone 2003). Different ADI approaches to deconstruct and subtract the stellar light are available, for example, the principal component based analysis (KLIP, PynPoint packages; Soummer et al. 2012; Amara and Quanz 2012), or locally optimized combination of images (LOCI package; Lafrenière et al. 2007).

ADI has the advantage compared to RDI that the stellar light contribution is determined from the science star data itself. However this comes with the disadvantage of signal suppression, often referred to as "self-subtraction". This is caused by the temporal overlap of the planet or disk signal with itself on the detector, and depends on the amount of field rotation that is achieved during the observations. The field rotation is given by the change of the parallactic angle and is a function of the observing time, the location of the observatory, the declination of the star and the local sidereal time. Long observations are needed, but in practice, the instrumental drift of the PSF and changing weather conditions are limiting factors (Cantalloube et al. 2019).

For point sources such as planets, this signal suppression can be well characterized by injection of model point sources into the data before reduction. This is however challenging in the case of extended disks with an unknown brightness distribution. A typical result is a strong signal suppression along the minor axis of the disk, leading to broken ring structures (Milli et al. 2012; Perrot et al. 2016; Ginski et al. 2016; de Boer et al. 2016). This effect also complicates the detection of embedded planets in disks.

The presence of extended disk signal leads to a higher noise floor in the ADI processed data. Extended disk signal can also lead to false-positive planet signals when confronted with aggressive post-processing. Rameau et al. (2017a) and Follette et al. (2017) demonstrated this effect for the prominent case of the HD100546 system for which multiple planet candidates were suggested in the past (Quanz et al. 2013a; Brittain et al. 2013; Currie et al. 2015). Signal suppression is a function of separation from the center of rotation as well as the inclination of the disk. The smaller the separation from the center and the smaller the inclination of the disk, the stronger is the signal suppression. Therefore, ADI is particularly ill suited to detect disks in face-on viewing geometry or small disks.

### 2.2.3. Polarization Differential Imaging.

The use of polarization differential imaging (PDI, Kuhn et al. 2001) successfully enabled the imaging of circumstellar disks. When stellar light is scattered off by dust grains, the resulting light is partially linearly polarized. The degree of linear polarization depends on the scattering angle between  $0^\circ$  (forward scattering) and  $180^\circ$  (backward scattering)<sup>2</sup>, and is typically peaking at  $90^\circ$ , i.e., close to the ansae of the disk. Figure 2 provides a schematic representation of stellar light scattered by a disk.

The latest generation of instruments include a polarizing beam-splitter or a non-polarizing beam-splitter combined with polarization filters (Tamura et al. 2006; Perrin et al. 2015; Schmid et al. 2018; de Boer et al. 2020). These are usually combined with a half-wave plate that modulates the polarization direction of the incoming light and allows to split it into two orthogonal, linearly polarized components, which are imaged simultaneously on the detector. Since the star exhibits only a low level of polarization, the stellar light will be nearly identical in both beams, while the polarized scattered light from the disk will differ. As the central star illuminates all directions of the surrounding disk, the disk will exhibit an azimuthal orientation of the electric field vector for single scattering events. This leads to a so-called "butterfly" pattern when one subtracts the two orthogonal polarized beams from each other, i.e., one polarization direction will show as two positive lobes in the image and the other as perpendicular aligned negative lobes. The strength of the PDI technique, is that as orthogonal polarized beams are recorded simultaneously or nearly simultaneously (depending on the instrumental design), there is no temporal variation of the instrument PSF. In addition, there is no signal self-subtraction as in ADI, due to the different polarization directions in each part of the disk.

The PDI technique follows the Stokes formalism (Stokes 1851), in which the polarization state is fully described by

<sup>2</sup>Note that in solar system research, the scattering angle is sometimes defined such that that  $0^\circ$  corresponds to backward scattering, not forward scattering. We use the convention that is commonly used in the context of light scattering theory and astronomical observations.

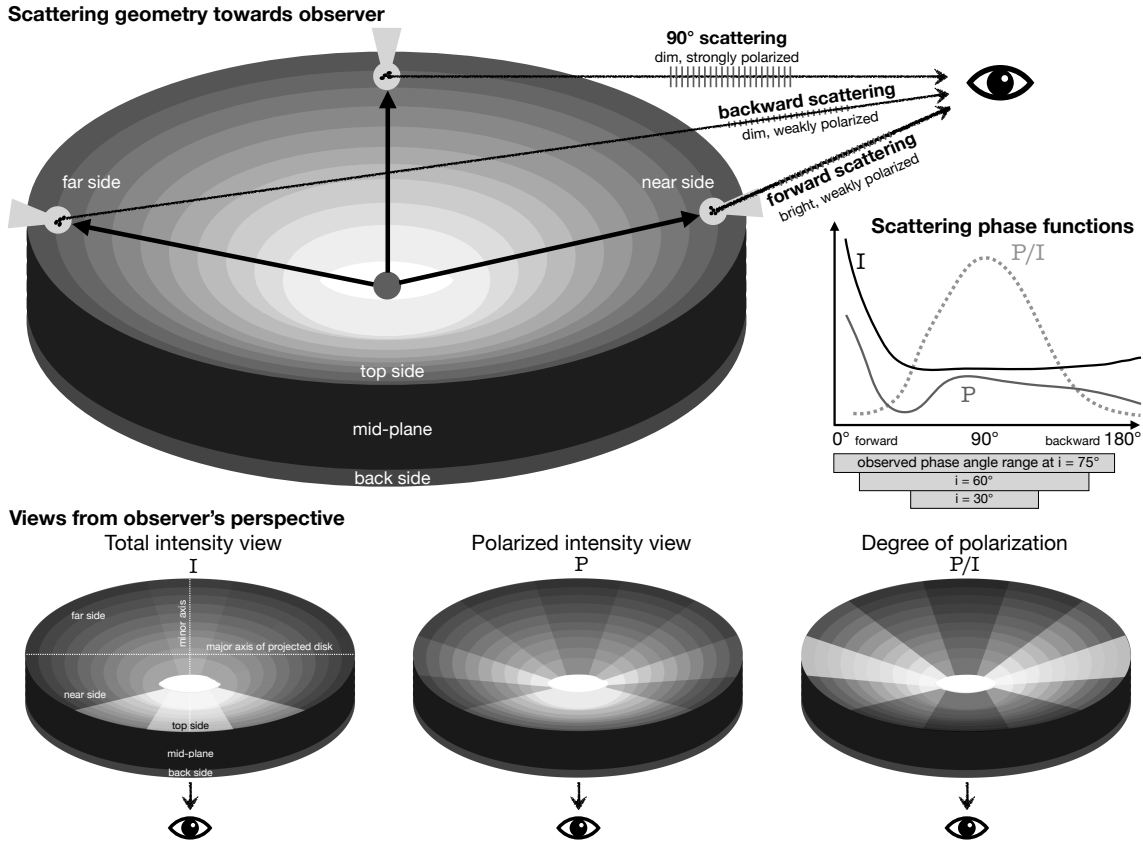


Fig. 2.— Schematic representation of the scattering geometry, viewing geometry and the influence of phase functions. The **top panel** shows the scattering locations in which forward ( $\approx 0^\circ$ ), backward ( $\approx 180^\circ$ ), and  $\approx 90^\circ$  scattering take place for a viewer that is off to the right-hand side. For the case of grains/aggregates that are somewhat *larger than the wavelengths of observation* (which seems to be typical for the studied disks), the key-hole symbols highlight the significant forward scattering enhancement at each scattering point. The total intensity  $I$  and polarized intensity  $P$  produced by the scattering event are sketched in **the plot**, showing the phase functions as a function of scattering angle from  $0^\circ$  (forward scattering) to  $180^\circ$  (backward scattering). Below the plot, we indicate the scattering angles that actually occur in a disk seen under specific inclinations, assuming a height of the scattering surface in the outer disk of  $0.15r$ . Note that the smallest scattering angle observable will actually be limited by the inner working angle of the observation. The **bottom row** shows the brightness variations of the disk surface one would expect just from the properties of the sketched phase functions, this time using the perspective of the reader, clearly showing the effects of enhanced forward scattering by large grains/aggregates. In contrast, in a disk in which *small (sub-micron) grains* are dominant, the intensity phase function will be nearly constant (isotropic scattering), and the intensity view would present a much more evenly bright disk surface. The polarized intensity would peak along the major axis of the projected disk ( $90^\circ$  scattering), resembling the degree of polarization view shown at the bottom right.

the Stokes vector  $S$ :

$$S = \begin{bmatrix} I \\ Q \\ U \\ V \end{bmatrix} \quad (1)$$

where  $I$  is the total intensity of the light,  $Q$  the vertical and horizontally linearly polarized light,  $U$  the linearly polarized light rotated with  $45^\circ$  with respect to  $Q$ , and  $V$  contains the circularly polarized light. The latter is typically not measured.  $Q$  and  $U$  images are obtained by rotating the astrophysical polarized signal into the frame of the polarizer or polarizing beam-splitter within the instrument. One major consideration when attempting to record any polarized signal is that reflections within the instrument will lead

to additional instrumental polarization (see *Snik and Keller 2013* for a detailed discussion). These can be partially cancelled by the so-called "double-difference" method (*Baguolo et al. 2009*) that records not only  $Q$  and  $U$  frames but  $Q^+$ ,  $Q^-$ ,  $U^+$  and  $U^-$ . The difference between  $Q^+$  and  $Q^-$  ( $U^+$  and  $U^-$ ) is that the HWP is rotated by  $45^\circ$ , which flips the sign of the incoming polarized signal, while instrumental polarization introduced downstream of the HWP retains its original sign. If the HWP is placed early in the path of light within the instrument, then a subtraction of  $Q^+$  and  $Q^-$  ( $U^+$  and  $U^-$ ) will cancel the majority of instrumental polarization, while the astrophysical signal is retained. However even using this method, some instrumental polarization, upstream of the HWP is retained. Furthermore, the stellar light itself may exhibit low levels of polarization,

due to interstellar dust or local dust. Both of these will significantly affect the contrast achievable with PDI and need to be removed. To do so, it is assumed that instrumental and stellar linear polarization will to first order be proportional to the total intensity of the stellar light. Thus the usual approach is to measure the total intensity and polarized intensity signal in an area of the image for which no disk signal is expected, or for which it is expected that the stellar and instrumental polarization signal will be dominant. One can then derive the proportionality factor between total and polarized intensity and subtract a thus scaled version of the total intensity image from the double difference corrected Stokes  $Q$  and  $U$  images. This removes simultaneously the remaining instrumental polarization and the stellar polarization. This critical technique was pioneered by *Canovas et al. (2011)* and *Hashimoto et al. (2012)* and is now a standard component of PDI image processing.

To obtain a polarized intensity image of the disk, one can combine the Stokes  $Q$  and  $U$  components  $PI = \sqrt{Q^2 + U^2}$ . However, as this involves squaring the  $Q$  and  $U$  images, the  $PI$  images often suffers from a faint halo in the areas most strongly affected by photon noise. It is therefore more convenient to instead use the azimuthal Stokes parameters (*Monnier et al. 2019; de Boer et al. 2020*):

$$\begin{aligned} Q_\phi &= -Q \cos(2\phi) - U \sin(2\phi) \\ U_\phi &= +Q \sin(2\phi) - U \cos(2\phi) \end{aligned} \quad (2)$$

where  $\phi$  is the azimuth angle in the image plane. Using this formalism all azimuthally polarized signal is positive in  $Q_\phi$  and radially polarized signal is negative in  $Q_\phi$ .  $U_\phi$  contains signal that is  $45^\circ$  offset from either polarization direction. In practice  $Q_\phi$  and  $PI$  are nearly identical, with the more favorable noise properties in the  $Q_\phi$  image. If the polarized light is due to single scattering events only,  $U_\phi$  contains no signal and can be used as a convenient noise estimator. However, this breaks down for disks seen under high inclination, where multiple scattering along the line of sight becomes a significant factor (*Canovas et al. 2015*).

PDI as a technique is now matured to the point that it can be used for the characterization of the innermost disk regions and directly imaged extrasolar planets. Asymmetric dust distributions in regions smaller than the telescope resolution element (e.g., inner disk, CPDs, planetary clouds) will introduce a residual polarization. These effects are generally small, on the order of 0.1-1% (*Stolker et al. 2017a*), but can become extreme, for edge-on viewing geometries as in the case of CS Cha b, which yielded a degree of linear polarization of  $13.7 \pm 0.4\%$  in the J-band (*Ginski et al. 2018*). Similarly, *van Holstein et al. (2021)* used unresolved polarimetric measurements of the sub-stellar companion in the DH Tau system to show that it must be surrounded by an accretion disk. These examples demonstrate the achieved maturity of the PDI technique, as well as the important insights that can be gained from the polarization state of unresolved sources.

#### 2.2.4. Spectral Differential Imaging.

A way to overcome temporal PSF variations is offered by spectral differential imaging (SDI). High contrast imaging instruments have integral field spectrographs (IFS) with low spectral resolution ( $R < 100$ ; *Claudi et al. 2008; Larkin et al. 2014; Groff et al. 2015*), providing images at different wavelengths. SDI is based on the fact that the stellar speckle halo scales radially with wavelength, while any continuum source remains nearly identical with wavelength. The stellar speckles can therefore be subtracted after rescaling the images, revealing the disk or planet signal. SDI has the advantage that images at all wavelengths are taken simultaneously, such that temporal PSF changes or changing weather conditions are not problematic anymore. However, this technique assumes that the instrument response is identical across wavelengths. This can be a problem in particular for ground based AO imagers, as the correction of the wavefront aberrations is wavelength-dependent with better correction obtained at longer wavelengths. In addition, the radial shift applied when re-scaling the images depends on the wavelength range covered by the instrument. Finally, SDI suffers from similar signal suppression effects as ADI imaging in the radial direction and is thus not ideal for the imaging of extended structures. At higher spectral resolution  $R > 1000$ , specific spectral lines can be resolved, and atmospheric or accretion tracers of young planets can be observed. This technique was used to detect the second protoplanet in the PDS 70 system, discussed in section 6.1.

### 2.3. Facilities and sample

Pioneering images of externally illuminated protoplanetary disks (proplyds) and disks seen in absorption against the bright nebular background were obtained in the Orion Nebula with the Hubble Space Telescopes (*O'Dell et al. 1993; O'Dell and Wen 1994*). As is clear from Figure 3, only a few disks had been imaged at the time of PPV (*Watson et al. 2007*), and most of them were edge-on disks seen in silhouette or very extended disks (e.g., *Grady et al. 2000, 2001; Krist et al. 2000; Stapelfeldt et al. 2003*). The time between PPV and PPVII marks the transition between space- and ground-based facilities as the main carrier of optical and near-IR images of protoplanetary disks, following pioneering work by *Roddi et al. (1996), Pantin et al. (2000), Kuhn et al. (2001), Itoh et al. (2002), and Apai et al. (2004)* with the University of Hawaii adaptive optics system, the Adaptive Optics Near IR System (ADONIS) at ESO, the United Kingdom IR Telescope (UKIRT), the Subaru/CIAO, and the VLT/NACO facilities, respectively. Nowadays, the vast majority of scattered light images at the optical and near-IR wavelengths are acquired with 8-m, AO- and polarimeter-equipped, telescopes, in particular with VLT, Subaru, and Gemini in PDI mode (see Sect.2.2).

The first instrument to perform systematic PDI observations of disks was the Subaru/HiCIAO instrument, through the SEEDS program that observed tens of protoplanetary

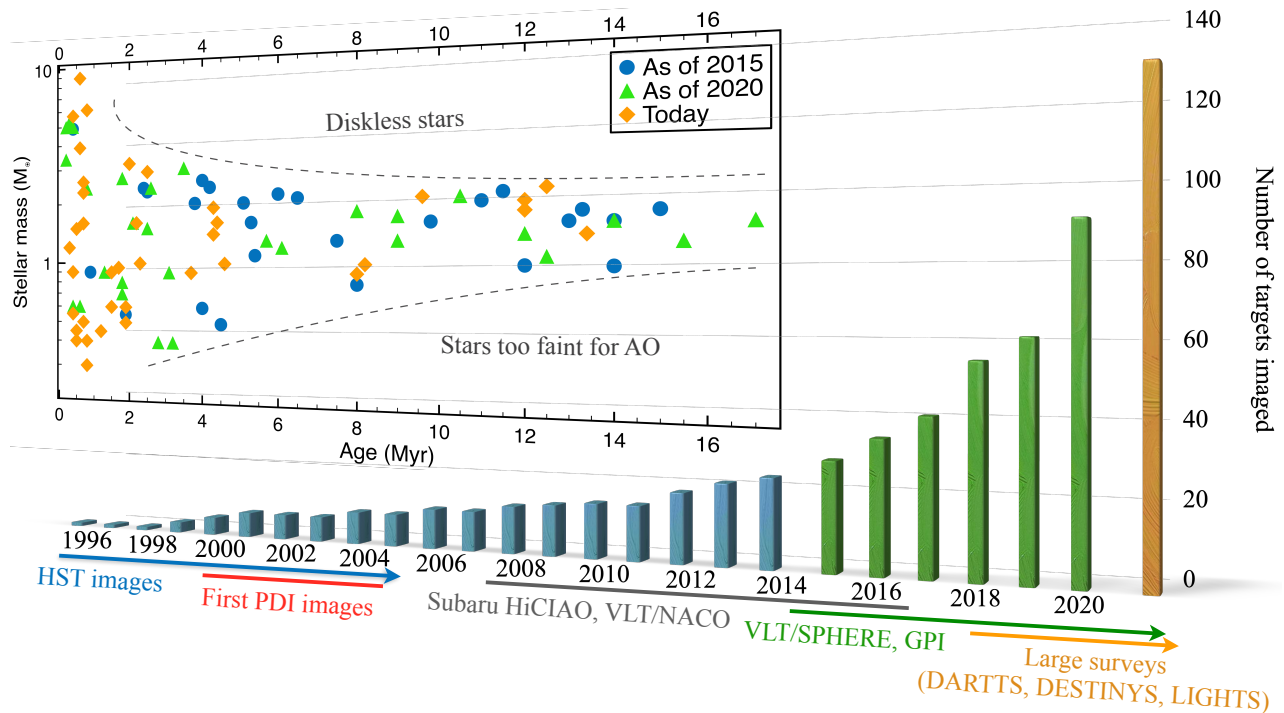


Fig. 3.— Total number of protoplanetary disks imaged per year. The count includes targets with observations (both detections and non-detections) that were published for the first time. The inset diagram shows the evolving range of stellar properties probed by the available sample. The count does not include proplyds and disks seen in silhouette.

disks, with 18 observations so-far published, half of which being bright T Tauri stars and the other half, Herbig Ae/Be stars (e.g., Hashimoto et al. 2012; Kusakabe et al. 2012; Mayama et al. 2012; Tani et al. 2012; Takami et al. 2013; Follette et al. 2013; Tamura 2016; Mayama et al. 2020). PDI was also successfully employed with VLT/NACO to image the disk around a handful of Herbig Ae stars (Quanz et al. 2011, 2012, 2013a; Canovas et al. 2013; Garufi et al. 2013, 2014; Avenhaus et al. 2014a,b). This first PDI campaign was limited by the performance of the AO system available at the time enabling detection of only bright disks (typically  $10^{-2}$  times the central star, see Sect. 4.1) around bright stars (typically  $R$  mag  $< 10$ ). As of 2015, the two dozens targets imaged with PDI were mainly  $1-3 M_{\odot}$  stars older than 4 Myr (see Figure 3, top), providing therefore a very biased sample.

The sample of observed targets was then significantly expanded with the advent of the extreme-AO system driving VLT/SPHERE (Beuzit et al. 2019) and GPI (Macintosh et al. 2014). Between 2015 and 2020, the sample size tripled, reaching more than a hundred. In addition, the range of stellar properties probed by these images stretched to younger ages (1–2 Myr) and lower mass ( $0.3 M_{\odot}$ , see Figure 3, top). The stability of the systems employed and the maturity of the post-processing techniques have motivated systematic observations performed under specific observing programs such as DARTTS-S (Disks ARound TTauri Stars with SPHERE, Avenhaus et al. 2018; Garufi et al. 2020), LIGHTS (Large Imaging with GPI Her-

big/TTauri Survey, Laws et al. 2020, Rich et al. in prep.), and DESTINYs (Disk Evolution Study Through Imaging of Nearby Young Stars, Ginski et al. 2020, 2021b).

Despite the significant progress in alleviating the sample bias, the stellar parameter space that is currently covered is still impacted by technical limitations. The minimum stellar brightness necessary to drive the AO at the telescope is in fact preventing us from accessing faint embedded young stars, the brown dwarf regime, and stars lighter than  $0.3 M_{\odot}$ . As is clear from Figure 3, the observed stars distribute in a sort of cusp with the upper desert due to absence of disks in old massive stars and the lower desert imposed by the current limits of AO guiding systems.

### 3. Theoretical background of disk substructures

To provide context for the observed substructures in disks we present a brief review on how such features could be generated. Both scattered light and sub-millimeter continuum emission in these sources are probing dust grains. The origin of the observed substructures in disks is therefore intimately related to the motion of dust particles embedded in a gaseous medium. As the gas moves at sub-Keplerian velocities, due to its pressure support, and the dust grains move at Keplerian velocities, a velocity difference exists between gas and dust grains. Drag forces then act on dust grains and influence their motions. Small grains are well coupled to the gas, and their distribution is expected to be representative of the distribution of the gas.

Regions where dust grains can be lifted high above the disk midplane (due to high surface density or strong vertical mixing) will be exposed to direct stellar light that can be scattered towards the observer. On the other hand, low densities and weak turbulent mixing remove grains from the direct exposure to stellar light, leading to dark regions in the disk, while drag forces will cause larger grains to move towards higher pressure regions. Long-term stable pressure maxima and minima (often implying surface density maxima and minima) will lead to variations in the distribution of both small and large grains, creating observable features at various tracers. The origin of these substructures is therefore related to the mechanisms that can produce long-term stable pressure variations. In the following, we provide a brief overview of such mechanisms.

### 3.1. Mechanisms not invoking planets

Radial gradients of temperature and density in a disk form condensation fronts, regions where the gas transitions from a gaseous to solid form. These condensation fronts typically contain water and carbon oxides. At these fronts the change in chemistry and opacity can lead to a non-monotonic pressure gradient, with the possibility to collect dust particles (*Ciesla and Cuzzi 2006*), or induce grain growth (*Zhang et al. 2015*). Using a hydrodynamical two-fluid approach it was suggested that an instability arises through the vertical settling of dust in protoplanetary disks which produce toroidal gas vortices that are able to collect dust in them, leading to observable ring-shaped features (*Lorén-Aguilar and Bate 2015*).

The formation of organized structures in disks has been seen also in a variety of magnetohydrodynamical (MHD) simulations, both in local and in global simulations. In this summary, we focus only on global simulations because the local simulations only yield spatial information on small scales of the order of the disk thickness (pressure scale height), while the observed features cover a large spatial extent. For more details, we refer the reader to the Chapter by *Lesur et al.* In non-ideal simulations that included a transition between a magnetically active region where turbulence is driven by the magneto-rotational instability (MRI) and a dead-zone, where non-ideal effects quench the MRI, *Ruge et al. (2016)* observed dust collection near the interface between the two regimes due to a presence of a pressure maximum. *Riols and Lesur (2019)* provide an overview of MHD simulations that show ring occurrence. Generally, configurations with net magnetic field can show ring-like features, even in the ideal-MHD case, where the rings represent themselves as a succession of sub-Keplerian and super-Keplerian bands (*Béthune et al. 2017*). In disks that are unstable to the MRI, *Béthune et al. (2016)* found self-organized toroidal structures in unstratified three-dimensional disks when including the Hall-effect in the MHD-equations. In global axisymmetric simulations using ambipolar diffusion *Riols et al. (2020b)* show that the

zonal flows (rings) are closely linked to the existence of a MHD wind. In their simulations, the ring width and separation is roughly compatible with observed features.

An important non-axisymmetric feature in disks are vortices, i.e., localized regions which, in a frame moving with the mean flow, show a reversed (anti-cyclonic) rotation. Such vortices are regions of increased density and pressure and small embedded dust particles will collect in them leading to observable, crescent-shaped features. In hydrodynamical disks without an embedded planet, two scenarios can lead to such vortices. The first is the subcritical baroclinic instability (SBI, *Klahr and Bodenheimer 2003; Lesur and Papaloizou 2010*), which requires a negative radial entropy gradient in the disk and finite amplitude perturbations. The second is the vertical shear instability (VSI, *Nelson et al. 2013; Barraza-Alfaro et al. 2021; Blanco et al. 2021*) suggested to generate turbulence in disks which requires a vertical gradient in the angular velocity and short cooling times. In thicker, nearly isothermal disks large scale vortices can be generated as shown in 3D hydrodynamical simulations (*Richard et al. 2016; Manger et al. 2020*).

### 3.2. Gap creation by planet-disk interactions

Planet-disk interactions can also trigger a variety of features that can be observed. This process is based on the effect that a planet created a wake that travels through the disk as a spiral wave.

Sufficiently massive planets embedded in a disk deplete the gas at the orbital location if the thermal and viscous criteria for gap-opening are met. Such an annular gap is caused by angular momentum transfer from the planet to the ambient gas induced by the spiral density arms that are created by the planet, as showed in full hydrodynamical simulations (*Bryden et al. 1999; Kley 1999*). The gap depth and width depend on the disk viscosity (*Crida et al. 2006*). Above a critical mass of few ten  $M_{\text{Earth}}$  (depending on the disk viscosity and temperature), density (pressure) maxima inside and outside the gaps exist. Dust can collect there and lead to the observed ring-like features where the dust density divergence exceeds that of the gas (*Paardekooper and Mellema 2006*).

A striking application of these ideas is the interpretation that possibly all the multiple rings observed in sub-millimeter observations are created by embedded planets (*Zhang et al. 2018; Lodato et al. 2019*). We refer to the Chapter by *Bae et al.* for a comparison with the exoplanet population. For several cases it was noted that one single planet is able to produce a multitude of rings (*Dong et al. 2017*). However, this effect turned out to be a consequence of the over-simplified thermodynamics used to describe the disk temperature in the simulations (often a power law for the temperature radial profile). The reason for the appearance of multiple rings was traced back to the locally isothermal approximation which results in an incorrect angular momentum transport in disks (*Miranda and Rafikov 2019*). *Zhang and Zhu (2020)* show that for a cool-



ing time that equals the dynamical timescale,  $\tau_{\text{cool}} \sim \Omega^{-1}$ , the strength of the spiral arms is weakest, while for shorter (more isothermal) or longer (more adiabatic) cooling the strengths of the spirals become stronger again. As a consequence the number of rings created by a single planet varies with the cooling timescale (Facchini et al. 2020). Ziampras et al. (2020a) showed in fully radiative simulations which included viscous and stellar heating that a multi-ring system such as the one observed in AS209 with ALMA (Guzmán et al. 2018) is better explained by multiple planets instead of a single one, emphasizing the need to consider radiative effects. If planetary migration is included, Wafflard-Fernandez and Baruteau (2020) showed that a single planet with different migrations speeds can in principle generate multiple rings in the dust distribution which are, however, slowly dissipating with time via disk turbulence. For more details on migration, we refer to the Chapter by Paardekooper et al.

### 3.3. Spiral waves

Spiral arms can be produced in disks, and such spiral arms can differ in their pitch angle  $\beta$ , which is the angle that the spiral makes with a circle around the star. First, a planet embedded in the disk will lead to wakes in the form of spiral arms that are sheared out by the Keplerian motion. The value of  $\beta$  is determined by the local temperature (sound speed) in the disk. Using linear theory, valid for planets lighter than the thermal mass,  $M_{\text{th}} \sim h^3 M_*$ , where  $h$  denotes the disk aspect ratio, the shape of the spirals was given for disks with constant  $h$  by Ogilvie and Lubow (2002); Muto et al. (2012). Deviations occur for massive planets where the spirals turn into strong shocks (Zhu et al. 2015) and when the heating by the spirals is included (Ziampras et al. 2020b). In these cases the pitch angle becomes larger. A second possibility would be a massive (stellar) companion object, that triggers the formation of tidal arms in the inner disk which appear as wide spirals with a large pitch angle (Dong et al. 2015b, 2016a). In a circumbinary disk, the gravitational torque exerted by the binary leads to the formation of a large eccentric inner cavity in the circumbinary disk with highly reduced mass and large asymmetric features can be produced in the disk such as blobs, eccentricities and spiral arms (see for example Thun et al. 2017; Ragusa et al. 2017; Keppler et al. 2020a). Another, third possibility, is the formation of spiral features in more massive disks where the disk’s own self-gravity cannot be neglected, usually for disk masses of about  $\sim 1/10$  of the stellar mass. In simulations that include disk self-gravity and a simplified cooling prescription it was shown using, Smoothed Particle Hydrodynamics (SPH) simulations that the disks settle to an equilibrium state where the induced turbulent heating by the spiral arms match the cooling rate where the Toomre parameter is unity  $Q \sim 1$  throughout the disk (Cossins et al. 2009). Additionally, in recent 3D grid simulations it was shown that the occurrence of the spiral arms is an intermittent process and the spirals do not show

long-term global coherence (Béthune et al. 2021). Both simulations indicate that the pitch angles are confined to a narrow range  $\beta \sim 15^\circ$ , relatively independent of the stellar mass and disk radius.

Planets can also induce non-axisymmetric features. As an annular gap is created by a massive planet, steep radial gradients of the surface density, pressure and a change in the rotational profile occur. This can trigger a Rossby-wave instability (RWI, Lovelace et al. 1999) near the gap edge creating a vortex (Li et al. 2005). Numerical studies have shown that vortex properties depend on various physical processes such as turbulent viscosity and disk self-gravity. Lower viscosity allows vortices to live longer (de Val-Borro et al. 2006), whereas the inclusion of self-gravity tends to weaken vortices, shortening their lifespan (Regály and Vorobyov 2017).

Most theoretical studies consider planets orbiting in the plane of the disk. However, the presence of a massive planetary or sub-stellar companion on an inclined orbit can induce a warp in the disk (Xiang-Gruess and Papaloizou 2013), and relative misalignment of specific disk radii. The condition for the tilting to occur is that the companion angular momentum is greater than the inner disk’s (Matsakos and Königl 2017). This is confirmed by 3D hydrodynamical simulations that show that in the case of an inclined planet, massive enough to carve an annular gap, the inner and outer disk can be misaligned (Nealon et al. 2018), and in some cases, the disk can have a higher inclination than the planet (Bitsch et al. 2013). If the mass ratio is high, in the extreme case of an equal mass stellar binary, the inner disk can break and freely precess (Facchini et al. 2013), leading to a variety of misalignment angles that could induce narrow or broad shadows on the outer disk (Facchini et al. 2018). Secular precession resonances in the case of high stellar-companion mass ratio can also lead to significant disk misalignments (Owen and Lai 2017). Finally, the Kozai-Lidov effect can bring a massive planet located within the cavity to a high inclination in the case of a multiple systems, like HD100453, inducing the misalignment of the inner disk (Martin et al. 2016; Gonzalez et al. 2020; Nealon et al. 2020; Ballabio et al. 2021).

## 4. Global structure of protoplanetary disks

In the following section, we review observational results that enabled to constrain the global disk structures, through their spatial extent in the IR scattered light and the apparent shape of the scattering surface. We also discuss how the dust grain properties directly affect the disk appearance.

### 4.1. Disk radial extent and brightness

In the following, we refer to ‘disk size’ as being the extent of the disk in scattered light. The first targets imaged in scattered light were small-scale reflection nebulae like T Tau (Nakajima and Golimowski 1995) and exceptionally bright and extended disks like AB Aurigae (Roddier et al. 1996; Weinberger et al. 1999; Grady et al. 1999).

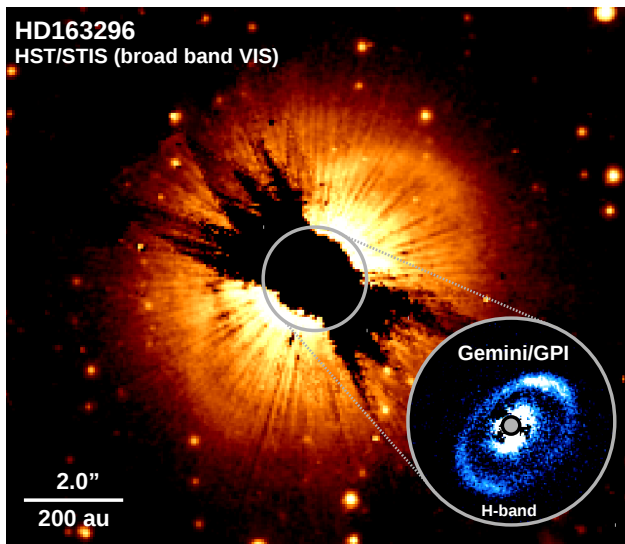


Fig. 4.— Hubble Space Telescope total intensity image of the disk surrounding the Herbig star HD 163296 taken at visible wavelength range with the Space Telescope Imaging Spectrograph (STIS). The masked center area was covered by a coronagraphic mask. We show a combination of all observation epochs presented in *Rich et al. (2020)*. Part of this data was first presented in *Grady et al. (2000)*. The circular inset shows Gemini/GPI polarized light data taken in the near-IR from *Monnier et al. (2017)*. While lacking the same inner working angle as modern ground based facilities, the HST data is sensitive to faint extended structures typically not detected from the ground.

Before 2010, only very large disks ( $>100$  au in size) such as HD163296 (see Figure 4) or SU Aur were observed with HST (*Grady et al. 2000, 2001, 2009; Krist et al. 2000; Pinte et al. 2008*), or as HD100546, with the first AO-systems (*Pantin et al. 2000; Kuhn et al. 2001; Fukagawa et al. 2006; Riaud et al. 2006*). AO-assisted observations from 8-m telescopes then detected a dozens disks of intermediate sizes (15–100 au in size, e.g., *Mayama et al. 2012; Thalmann et al. 2015; Rapson et al. 2015*), some that were previously undetected in HST surveys (*Grady et al. 2005*). The successful observations of disks of intermediate sizes is due to the fact that their extent corresponds to separations of  $0.1''$ – $0.7''$ , where the stellar illumination is still significant and both the angular resolution and sensitivity achieved by current ground-based telescopes are optimal to probe the disk. On the other hand, the common employment of a coronagraph for this type of observation prevents the access to separations (and therefore disk extent) smaller than  $0.1''$ – $0.15''$ . The first attempt to characterize small disks ( $<15$  au in extent) has recently been made with high-precision polarimetry, as mentioned in Section 2.2. The polarization state of unresolved light can be measured if the instrumental polarization and cross-talk are corrected with sufficient accuracy (*van Holstein et al. 2020*). The determination of the degree and angle of linear polarization from unresolved

emission together with radiative transfer modeling allows one to infer the presence, orientation, and potentially inclination of unresolved disks around the primary star (*Kepler et al. 2018; Garufi et al. 2020*) or around sub-stellar companions (*Ginski et al. 2018; van Holstein et al. 2021*).

While the diversity of disk sizes can be appreciated from near-IR imaging, the determination of the disk extent solely based on a sub-set of images is questionable. An illustrative case in this regard is HD163296 (Figure 4), where the disk is detected out to more than 500 au from HST images (*Wisniewski et al. 2008*) and to 440 au from Subaru/CIAO images (*Fukagawa et al. 2010*) but to less than 100 au from SPHERE and GPI (*Muro-Arena et al. 2018; Monnier et al. 2017*). A similar difference between HST and SPHERE images was reported for 2MASS J1609-1908 and 2MASS J1614-1906 (*Garufi et al. 2020; Walker et al. 2021*). This discrepancy is due to the modest sensitivity of polarimetric observations from the ground as the polarized light is only a fraction of the total scattered light (see Sect. 4.3). In general, the disk outer radius with detectable signal is strongly related to the amount of detectable photons in polarized scattered light. The observable amount of scattered light from a circumstellar disk is determined by the following factors, summarized in Figure 2: (i) the number of photons that reach the disk surface, governed by the stellar luminosity and by the possible presence of disk material shadowing the outer disk regions (see Sect. 5.2); (ii) the overall efficiency of dust grains in scattering photons at a specific wavelength (the dust albedo); (iii) the disk geometry and the scattering phase function, as these two elements determine the fraction of photons scattered in the direction of the observer (*Mulders et al. 2013*); (iv) in case of polarimetric observations, the polarizing efficiency of scattering particles (see Sect. 4.3; e.g., *Murakawa 2010*).

The disk brightness in scattered light can be measured comparing the surface brightness of the disk  $S_{\text{scat}}$  with the stellar flux  $F_*$  measured from the same set of images, which defines a brightness measure that is independent from the luminosity. The typical ratio between the  $S_{\text{scat}}$  integrated over the entire disk and  $F_*$  is around  $10^{-2}$  (e.g., *Fukagawa et al. 2010*). However, to measure the local capability of the disk to scatter the stellar radiation, we need to consider that the illumination from the star scales as a function of distance  $r$  as  $1/(4\pi r^2)$ . Therefore, we define  $\alpha_{\text{scat}}$  as the ratio of the surface brightness relative to the measured stellar flux as:

$$\alpha_{\text{scat}}(r) = S_{\text{scat}}(r) \cdot \frac{4\pi r^2}{F_*} \quad (3)$$

To alleviate the dependence of the observed brightness on the disk inclination (through the scattering phase function), the  $S_{\text{scat}}$  can be measured along the disk major axis where all observed photons are scattered by angles close to  $90^\circ$ . Also, to obtain a unique value representative of a disk, the contrast can be averaged between the innermost and outermost radii with detectable signal  $r_{\text{in}}$  and  $r_{\text{out}}$ . The scattered-to-stellar light contrast  $\alpha_{\text{scat}}$  thus calculated is

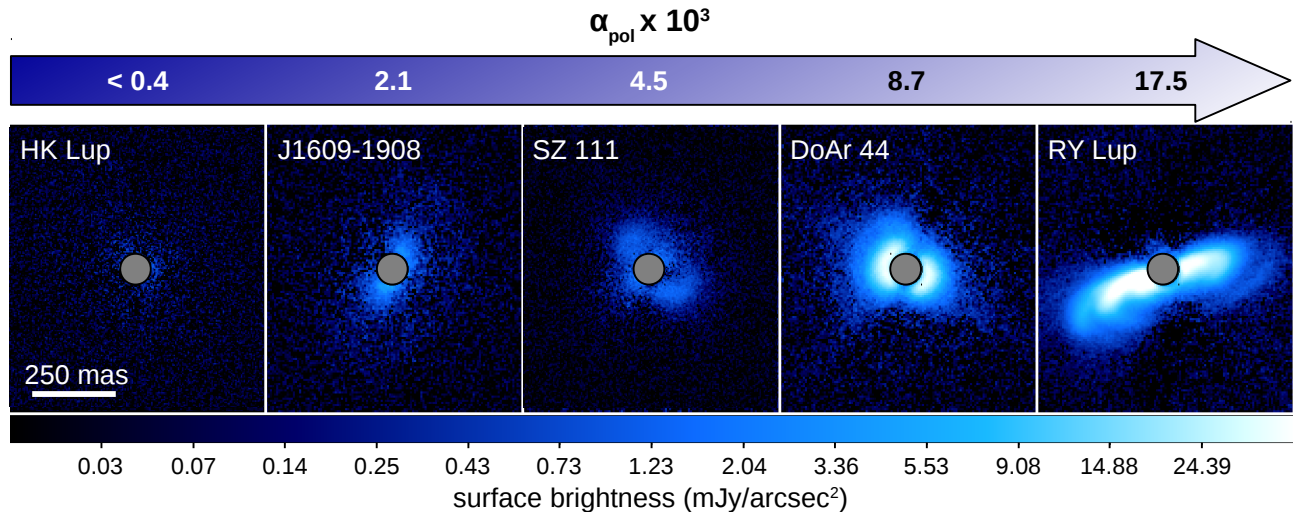


Fig. 5.— Disks observed with VLT/SPHERE sorted by polarized-to-stellar light contrast  $\alpha_{\text{pol}}$  (see Eq. 5) with increasing disk brightness from left to right. All images are using the same absolute color map. References are listed in Appendix A.

then:

$$\alpha_{\text{scat}} = \frac{1}{r_{\text{out}} - r_{\text{in}}} \cdot \int_{r_{\text{in}}}^{r_{\text{out}}} S_{\text{scat}}(r) \cdot \frac{4\pi r^2}{F_*} dr \quad (4)$$

If the scattered-light images are polarimetric, the polarized-to-stellar light contrast  $\alpha_{\text{pol}}$  from the observed polarized surface density  $S_{\text{pol}}$  is therefore similarly:

$$\alpha_{\text{pol}} = \frac{1}{r_{\text{out}} - r_{\text{in}}} \cdot \int_{r_{\text{in}}}^{r_{\text{out}}} S_{\text{pol}}(r) \cdot \frac{4\pi r^2}{F_*} dr \quad (5)$$

This measurement expresses the fraction of photons released by the star that are effectively scattered and polarized by the resolved portion of the disk. *Garufi et al.* (2017, 2021) measured the  $\alpha_{\text{pol}}$  for a large number of disks finding values from few times  $10^{-4}$  to few times  $10^{-2}$  (the current detection limit for any disk being  $\alpha_{\text{pol}} \sim 3 \times 10^{-4}$ ). Figure 5 provides the values of a few illustrative sources. We classify targets into three categories: faint disks ( $\alpha_{\text{pol}} < 10^{-3}$  typically corresponding to peak brightness of less than a  $\text{mJy/arcsec}^2$ ), moderately bright disks ( $\alpha_{\text{pol}} \sim 10^{-3} - 10^{-2}$  and peak brightness of few  $\text{mJy/arcsec}^2$ ) and bright disks ( $\alpha_{\text{pol}} > 10^{-2}$  and peak brightness of tens  $\text{mJy/arcsec}^2$ ).

A clear dichotomy between bright and faint disks was already found in early scattered light observations of Herbig AeBe stars (*Grady et al.* 2005), that detected far-IR bright disks (so-called Group I; *Meeus et al.* 2001) while far-IR faint (Group II) yield non-detections. This was originally interpreted as tracing differences in the geometry of the outer disk, with flared vs flat disks, respectively. However, recent studies found that Group I sources host disks with a large cavity ( $>10$  au), imaged at near-IR or millimeter wavelengths (*Maaskant et al.* 2013; *Garufi et al.* 2014; *Honda et al.* 2015). In general, this work shows a clear correspondence between a high disk brightness and the presence of a dust-depleted cavity, suggesting that the scattered

light brightness and the flared structure of the outer disk is related to the directly illuminated (and therefore bright) outer cavity edge of the disk.

Intermediate and large disks ( $>15$  au) that appear faint in scattered light can be explained by (partial) self-shadowing (*Dullemond et al.* 2002). The observed anti-correlation between the disk brightness and the thermal near-IR excess from the SED (*Garufi et al.* 2022) supports a view where, in these objects, the disk inner rim at the dust sublimation front is puffed up (*Dullemond et al.* 2001), and leaves the outer disk in penumbra (*Dong et al.* 2015a). A clear example is the non-detection of HK Lup in polarized scattered light (*Garufi et al.* 2020, see Figure 5) despite its large disk extent and brightness seen with ALMA (*Ansdell et al.* 2016). The distribution of the disk brightness appears uniform across M-to-A spectral types (*Garufi et al.* 2022), and given the bias of the current census (see Sects. 2 and 5.3), self-shadowed disks may be quite common.

As explained above, the measurement of the disk extent in scattered light depends on many factors. In addition to those previously mentioned regarding telescope sensitivity, scattering properties and disk geometry, the intrinsic vertical distribution of small grains in the disk upper layers, controlled by the turbulent mixing, may be another key factor. Scattered light measurements can therefore not be used to estimate the *physical* disk extent, that should be measured in an optically thin gas tracer of the bulk disk density with ALMA. For more details on this topic, we refer to the Chapter by *Miotello et al.*

## 4.2. Shape of the disk surface

A disk in hydrostatic equilibrium directly exposed to the stellar radiation is expected to exhibit a flaring surface (e.g., *Chiang and Goldreich* 1997). Such a geometry was proposed by *Kenyon and Hartmann* (1987) based on the large

thermal IR excess of YSOs and confirmed with Hubble observations showing the disk silhouette (e.g., *Burrows et al.* 1996; *Padgett et al.* 1999). Constraining the exact shape of the disk surface is fundamental to obtain a comprehensive view of the thermal and chemical structure of the disk. Scattered-light images (along with images taken in PAH emission features, *Lagage et al.* 2006) are among the best methods to measure the surface shape as, in optically thick disks, the observed photons are scattered by the uppermost disk layer. Observations of disk seen edge-on provide a direct measurement of the surface height (*Stapelfeldt et al.* 1998, 2014; *Villenave et al.* 2020). This type of observation is typically not possible for ground-based telescopes because the star needed to drive the AO system is masked by the disk itself and is thus faint at optical or even near-IR wavelengths. However, there are a growing number of objects, observed from the ground, for which the backside of the disk is visible as forward scattering peak below the dark midplane (see Figure 1 for some examples). When the disk midplane appears as a dark lane separating the observable front and rear disk faces (e.g. IM Lup and DoAr 25; *Avenhaus et al.* 2018; *Garufi et al.* 2020), the  $H(r)$  can be roughly measured from its width, and is found to be very large in the outskirts of such extended disks ( $\sim 70$  au at  $r = 300$  au). These measurements can be refined by combination with dedicated radiative transfer models (e.g., *Villenave et al.* 2019).

More generally the disk surface height can be inferred from the structures traced in the image, assuming that the disk is not eccentric. This is due to the fact that the typical flared and thus "bowl-shaped" surface of the disk will produce apparent offsets of disk structures along the minor axis, when viewed under an inclination. This effect is readily visible in our schematic figure 2, where the rim of the near-side of the disk appears much closer to the central star than the rim of the far-side. This well known projection effect has been used by *Silber et al.* (2000) and *Duchêne et al.* (2004) to measure the surface height of the GG Tau circumbinary disk, by tracing its inner rim at the edge of the central cavity. The same method can in principle be applied by tracing the outer rim of compact disks. This method becomes particularly powerful in disks with multiple rings (*de Boer et al.* 2016). In these cases the overall shape of the surface  $H(r)$  can be measured as a function of the separation from the central star and its flaring parameter (tracing the evolution of  $H(r)$  with  $r$ ) can be fitted. However, fitting approaches can cause significant discrepancy in the measure of the scattering height. For example, in HD97048, *Ginski et al.* (2016) measured a height of 18.5 au at 100 au, with a flaring index of  $1.73 \pm 0.05$  while *Rich et al.* (2021) find a larger value of  $2.48_{-0.3}^{+1.52}$ . This discrepancy is due to the fact that the former study concentrated on the sharp-peaked, forward scattering side of the ring for the extraction of the ring offset and semi-major axis, while the latter considered also the far side. The reasoning behind the different approaches was that the disk far side is marginally radially resolved and thus some ambiguity may be introduced whether one traces

the same height throughout the ring. It may well be possible that the true  $H(r)$  function lies in between the reported results. On the same target, the height of the emission of polycyclic aromatic hydrocarbons (PAH) was inferred to be  $\sim 34$  au at 100 au with a flaring index of  $1.26 \pm 0.05$  (*Lagage et al.* 2006). *Avenhaus et al.* (2018) applied this method to five bright T Tauri disks, finding flaring index values ranging between  $\sim 1.1$  and  $\sim 1.6$ , and that the individual rings of the various disks could be fitted by an individual flaring index of 1.21 with  $H(r = 100 \text{ au}) = 15.8$  au.

Obviously this method can only be applied to disks that show regular ring structures, and excludes those who have complex substructures (*Laws et al.* 2020). In these cases the height of the scattering surface may be inferred from measuring the scattering phase function of the dust particles. However a good knowledge of the disk surface is a priori needed to correct for the projection effects to measure the real scattering angles (*Stolker et al.* 2016b). This degeneracy can in principle be broken with detailed radiative transfer modelling as shown for example by *Takami et al.* (2014); *Dong et al.* (2016b). These simulations on the other hand depend on our knowledge of the dust scattering phase functions, which, as we discuss in Sect. 4.3 is still poor.

*Rich et al.* (2021) complemented this method with complementary measurement of the gas emission surfaces as observed with ALMA in the  $^{12}\text{CO}$  gas line in three disks. Such measurements can constrain the level of coupling between the small grains and the gas, as well as the turbulent mixing distributing small grains in the upper surface layers. They find that in two disks, the  $^{12}\text{CO}$  and scattering surface are similar at small radii, but that at large distance, the scattering surface is lower than  $^{12}\text{CO}$  emission surface, while for the third object, the two surfaces are similar. Radiative transfer modeling shows that a large gas-to-dust ratio could be responsible for the surface height differences, as well as changes in the physical conditions in the disk such as local heating due to a planet. Depending on the (molecular, dust) tracer considered the measured emission height will differ, and this is strongly dependent on temperature (for gas line as  $^{12}\text{CO}$ ) and on dust properties (for scattered light).

We note that these disk surface measurements are only available on bright disks. Little is known about self-shadowed disks, for which the  $H(r)$  of the disk regions in the penumbra are expected to be significantly lower. Measurements of these values and an actual distribution of values across an unbiased sample of disks is currently unavailable due to the difficulty in observing these faint disks. Similarly, the scattering surface shape is typically unknown for disks with complex morphology.

### 4.3. Dust properties

Most parts of the disks are optically thick at optical and near-IR light, and therefore, scattered light observations trace dust in the upper layers of disks, often several pressure scale heights above the midplane (*Chiang and Goldreich* 1997; *Lagage et al.* 2006). The dust in these regions



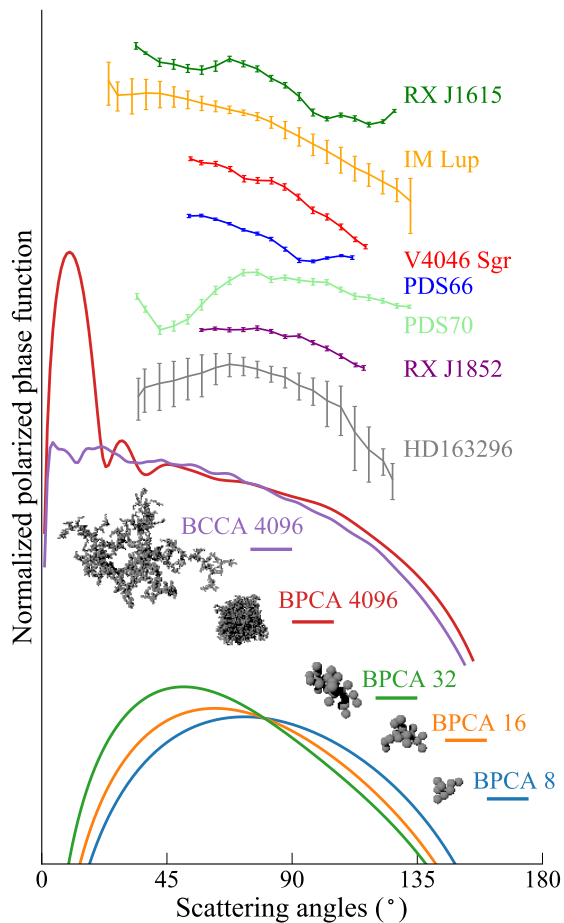


Fig. 6.— Polarized phase functions extracted from  $H$ -band observations (lines with error bars; Ginski et al. in prep.), compared with the T-Matrix light scattering simulations (full lines; Tazaki et al. in prep.). The upper set of theoretical curves correspond to dust aggregates consisting of 4096 monomers of radius of  $0.1 \mu\text{m}$  with resultant aggregate radii of approximately  $10 \mu\text{m}$  (BCCA; an open structure aggregate) and  $3.1 \mu\text{m}$  (BPCA; a compact structure aggregate). The lower set of curves is for smaller dust aggregates consisting of 8, 16, 32 monomers with resultant aggregate radii of 3.3, 4.5,  $6.0 \mu\text{m}$ , respectively.

should be well-coupled to the gas, with slow settling processes and efficient vertical mixing processes. This means that the dust should be either small individual grains (Dong et al. 2012b), or porous, possibly fractal aggregates. Models of dust aggregation generally show that aggregation is fast (Dullemond and Dominik 2005; Okuzumi et al. 2012), and that the velocities needed to destroy aggregates in collisions are only reached when these aggregates become large enough to start decoupling dynamically from the gas (Birnstiel et al. 2010), so there are good reasons to expect the dust in the disk surface to be present on the form of aggregates. However, fragmentation and infall of molecular cloud material can replenish small individual particles to some degree, so observational tracers are needed to determine the properties of the dust. Here, we focus much of our discussion of dust properties of optical properties of aggregates.

Information about the properties of the dust is encoded in the intensity and degree of polarization of the reflected light, in the angular dependence of these quantities (phase functions), and in the wavelength dependence (e.g. Takami et al. 2014). Grains with sizes much smaller than the wavelength of the observations scatter isotropically, with a bell-shaped polarization fraction peaking around a scattering angle of  $90^\circ$  (see Figure 2). The degree of polarization at the peak can get quite high, typically 20 to 70% (Krivova et al. 2000; Silber et al. 2000; Graham et al. 2007; Perrin et al. 2009; Murakawa et al. 2008; Tanii et al. 2012; Poteet et al. 2018; Monnier et al. 2019; Hunziker et al. 2021; Tschudi and Schmid 2021) and should be considered a lower limit since multiple scattering or limited resolution would tend to reduce the measured degree of polarization. Larger grains concentrate more of the scattered light into a small angle around forward-scattering direction, with smaller degrees of polarization, still bell-shaped around  $90^\circ$ . Aggregates can behave like large grains when it comes to the amount of forward scattering (Kozasa et al. 1993).

As discussed by Tazaki et al. (2019), aggregate sizes can be derived from the ratio of the forward and backward scattering intensity. If the aggregates are larger than the observing wavelength, then the polarization fraction is a measure of the porousness of the aggregates, with higher polarization degrees indicating higher porosity. The color of total and polarized intensity images indicate dust properties as well, with porous aggregates leading to gray or slightly blue colors, while more compact aggregates cause reddish colors in total intensity (Mulders et al. 2013).

For *intensity phase curves*, many sources do indeed show significant forward scattering enhancements (e.g. Quanz et al. 2011; Hashimoto et al. 2012; Kusakabe et al. 2012; Mulders et al. 2013; Ginski et al. 2016). When a full range from small to large scattering angles can be probed (see also see Figure 2), in both protoplanetary and in debris disks, the phase function is usually characterized by a very strong forward scattering peak, a somewhat flat region around 90 degrees, and a rise toward backward scattering (e.g. Hughes et al. 2018; Milli et al. 2017; Stolker et al. 2016a), consistent with lab measurements of large, porous aggregates (Muñoz et al. 2017). *Polarized phase functions* have now been measured for a number of disks, over significant ranges in scattering angle (Figure 6). Such polarized phase functions depend sensitively on aggregate radii. Smaller aggregates show a symmetric polarized phase function with respect to a scattering angle of  $90^\circ$ . In contrast, larger aggregates tend to develop forward scattering component. Aggregate structure also affects how strongly the forward scattering peak is expressed. Looking at the observations in Figure 6, there seem to be two classes of polarized phase functions. One is a smoothly increasing phase function for smaller scattering angles, such as IM Lup, V4046 Sgr, RX J1852. This class of phase function shows a very strong resemblance to the polarized phase functions of large ( $\gtrsim \mu\text{m}$ ) highly porous aggregates. The other class is a phase function with a strong drop-off at

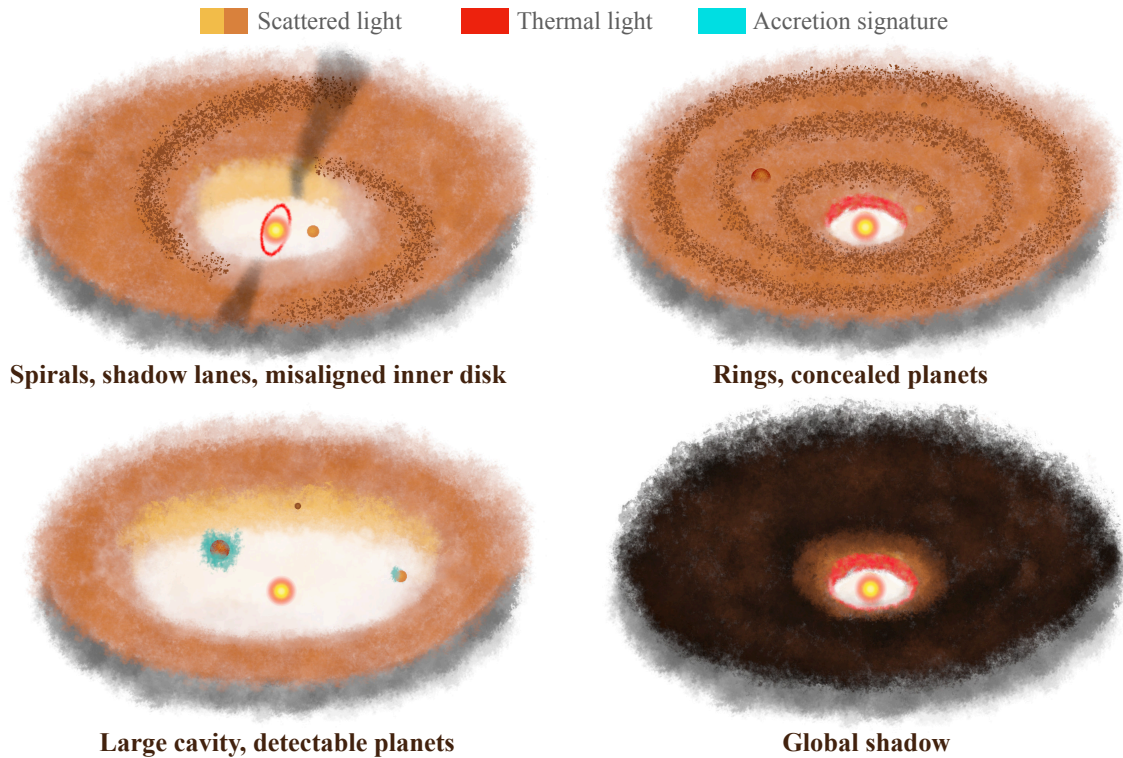


Fig. 7.— Visual synopsis of the topics treated in Sect. 5 and 6. Disk substructures such as cavities, rings, and spirals are discussed in Sect. 5.1, shadows and misaligned inner disk in Sect. 5.2, while protoplanets and accretion signatures in Sects. 6.1 and 6.2.

small scattering angles, such as PDS 70, HD 163296. Here, the increase in scattering intensity is not able to compensate the decrease in polarization fraction, leading to a drop in the polarized phase functions toward these forward-scattering angles. Such a functional shape can be well reproduced with very small aggregates ( $\lesssim \mu\text{m}$ ), or perhaps larger but very compact aggregates/particles.

The dust material can imprint its solid-state features in the scattered light as well. This should in principle give the most direct access to the grain composition, but this approach is limited by the small number of usable solid state features in the optical and near IR range. So far, scattered light displaying the water ice feature at  $3\mu\text{m}$  has been detected in HD 142527 (Honda *et al.* 2009) and HD 100546 (Honda *et al.* 2016). A detailed study of the ice feature observed in HD 142527 shows that the dust has an ice/core mass ratio between 0.06 and 0.2 (Tazaki *et al.* 2021), where the core was assumed to be made of silicate but may also contain other components that do not show an absorption feature at that wavelength.

## 5. Substructures

Since PPVI, near-IR and ALMA high angular resolution images have shown that disk substructures are very frequent, appearing as dust depleted cavities, rings, gaps, asymmetries and spiral arms. Figure 7 is a sketch of such substructures and of the topics discussed in this section.

### 5.1. Cavities, rings, spirals

#### 5.1.1. Cavities

The existence of large ( $> 10$  au) regions devoid of, or with significantly dimmed amount of dust grains was first predicted from the lack of near- and mid-IR excess from the SED (Strom *et al.* 1989). These objects were initially defined as transition disks (referred to as “transitional disks” in the PPVI review of Espaillat *et al.* (2014)) since it was believed that they were rapidly converting inside-out from a dust-rich to a dust-poor composition. The first resolved images were obtained for the extraordinarily large cavities of the multiple systems GG Tau (Dutrey *et al.* 1994, with the IRAM interferometer) and HD142527 (Fukagawa *et al.* 2006, with Subaru/CIAO). Cavities are now routinely resolved by PDI observations (e.g., Mayama *et al.* 2012; Hashimoto *et al.* 2012). However, in many cases the near-IR cavity is either smaller than when measured at millimeter wavelengths (e.g., Garufi *et al.* 2013; Villenave *et al.* 2019; Maucó *et al.* 2020) or undetectable at radii down to coronagraph (typically at 10–15 au; e.g., Benisty *et al.* 2015; Ginski *et al.* 2016; Muro-Arena *et al.* 2020). This spatial segregation of dust size is currently best explained by the existence of dust trapping of mm-sized pebbles at a local pressure maximum induced by a planetary companion (Pinilla *et al.* 2012). In this scenario, gas still flows through the cavity and carries well-coupled small grains with it. Therefore, one naturally expects a radial segregation between small and large grains (de Juan Ovelar *et al.* 2013)



that may be used to predict the position and the properties (mass) of a putative planetary companion responsible for the cavity (for a given disk viscosity).

### 5.1.2. Rings

Multiple rings in PDI were first detected in the Herbig Ae star HD169142 with early NACO observations that revealed the presence of two rings (Quanz et al. 2013b). Subsequent observations of the same disk with more advanced instrumentation indicated that the first ring is highly structured (Pohl et al. 2017) with asymmetric clumps distributed along the ring that rotate at Keplerian rotation (Gratton et al. 2019). Multi wavelength scattered light observations in the J and H bands can show a differential color for the two rings indicating that the stellar light hitting the outer disk has been reddened while traversing the first ring (Monnier et al. 2017). Subsequent observations of T Tauri and Herbig Ae stars indicated that multiple rings are quite common in T Tauri disks (e.g., Rapson et al. 2015; Thalmann et al. 2016; Monnier et al. 2017; Muro-Arena et al. 2018; Avenhaus et al. 2018; Bertrang et al. 2018). Overall, rings are found at all radii accessible to direct imaging, that is from the inner working angle (van Boekel et al. 2017), to the outermost radius probed at the given sensitivity (de Boer et al. 2016). Using analytical prescriptions for the gap morphology (Kanagawa et al. 2015) or hydrodynamical simulations followed with radiative transfer (Dong and Fung 2017), the properties of the annular gaps (width, depth) are related to the presence of massive planets for a given disk viscosity which can then be compared to current detection limits (Asensio-Torres et al. 2021, see Sect. 6.2). Other explanations are provided, for the presence of rings seen in the surface layers, for example ice lines (Okuzumi et al. 2012) of different volatile species. They can perturb dust dynamics locally which has a direct observational consequence (Pinilla et al. 2017). Pohl et al. (2017) compared the location of the snow line for various volatile species and found that for HD169142, the outermost gap could be explained by dust accumulation close to the CO ice line. This study has unfortunately not been done on a larger sample of rings and a morphological and statistical study of the rings properties in a large survey of T Tauri stars, in terms of spatial distribution, width, and contrast still remains to be done to infer whether they have a similar origin.

Many of the disks that show multiple rings in the submillimeter also exhibit rings in IR scattered light (see Chapter Bae et al.). However, there is no general correspondence between the location of the rings in the sub-millimeter and in the IR, nor in the numbers of rings detected. One of the clearest example is TW Hya (van Boekel et al. 2017; Andrews et al. 2016), as showed in Figure 8, panels c and d, not only the radial extent of the small grains distribution (seen in IR) differs strongly from the one of the large grains (seen with ALMA) but the annular gap/rings location do not match. This, in addition to providing a textbook

example of radial drift in disks, shows the difference in dust/gas coupling and that the disk can be highly structured beyond what is evident from sub-millimeter images. Muro-Arena et al. (2018) showed that in the case of HD163296, only one of the two rings imaged by ALMA (Isella et al. 2018) is detected in VLT/SPHERE observations. As the second, further, ring is not detected in scattered light, a natural explanation is that it lies in the shadow of the first ring, and must be significantly settled. These studies show that the analysis of a single dataset, obtained within a single wavelength regime, provides limited information and that it is crucial to perform a multi-wavelength analysis of these disks to constrain the mechanisms at play. Such a multi-wavelength approach can for example address the efficiency of dust evolution processes (radial drift, dust settling), as showed by the modeling of highly inclined disks at these two wavelengths (Villenave et al. 2019, 2020).

### 5.1.3. Spirals

Figure 9 provides images of disks presenting spiral features, that can be separated into various categories based on their morphology and on their possible origin. Some disks show two nearly symmetric arms (e.g., Grady et al. 2013; Wagner et al. 2015; Benisty et al. 2015; Stolker et al. 2016b). Juhász et al. (2015) showed that these spirals are likely tracing local perturbation of the disk scale height, rather than the density perturbations, and that in general opening angles are too large to be accounted by a companion located inwards of these spirals. This issue can be solved by considering a massive companion located beyond the spiral arms in the outer disk outside of the disk (Dong et al. 2015a). However, these massive planets have not been detected. Recently, Calcino et al. (2020) found that a  $10 M_{\text{Jup}}$  planet orbiting within the cavity on an eccentric orbit could account for the properties of the spiral arms.

Other disks show multiple asymmetric arms that may sometimes appear flocculent (e.g. Monnier et al. 2017). While it is unclear whether this can be the origin in all cases, some of these targets are known circumbinary disks for which spiral arms are triggered by the interaction of the disk with the stellar system within (e.g., Price et al. 2018; Monnier et al. 2019). In other cases, e.g., HD34282 or CQ Tau (e.g. Uyama et al. 2020; de Boer et al. 2021), the overall disk surface geometry might lead to apparent complex structures. Impressive, complex, and multiple spiral arms are observed in systems that show clear interaction with the surrounding material, possible remnant of envelope (as in e.g., AB Aur and DR Tau, Boccaletti et al. 2020a; Mesa et al. 2022), and for which the synergy with ALMA observations is once more essential. In SU Aur, for example, the geometry of the infalling material could be determined thanks to the combined analysis of IR scattered light and ALMA gas tracers (Ginski et al. 2021b). Another category includes large scale spiral arms that are due to the dynamical interaction of the disk with a known external compan-

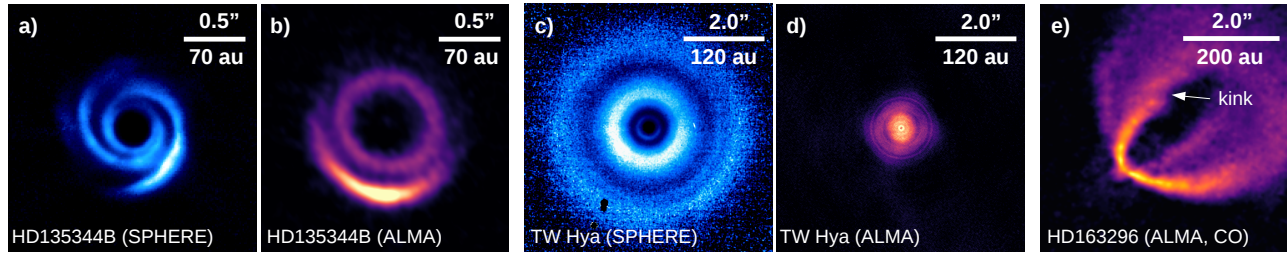


Fig. 8.— Comparison of IR scattered light images with ALMA observations. Panels (a)(b) for HD135344B, Panels (c)(d) for TW Hya. Panel (e) shows the detection of a non-Keplerian feature (so-called kink) in a channel map of the CO observations of HD163296.

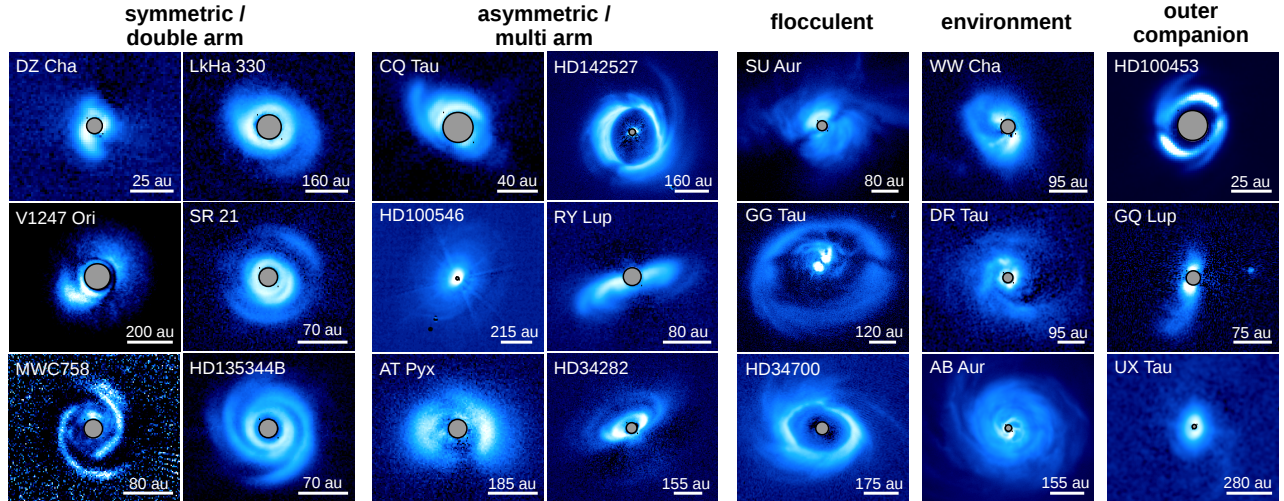


Fig. 9.— Spiral features imaged in scattered light at the time of this review. The majority of the data was taken with VLT/SPHERE with the exception of HD 34700, which was imaged with Gemini/GPI and LkHa 330 and V1247 Ori which were imaged with Subaru/HiCIAO. All relevant references for individual systems are listed in appendix A. All data were taken in the IR J and H-bands with the exception of LkHa 330 and MWC 758 which were imaged in the K and Y-band respectively. Color bars were individually adjusted to highlight the disk morphology. Categories are based on the spirals appearance alone, as the driving mechanism behind the spirals is still unclear (we do however list disks with a known outer companion in a separate category). We note that for several disks in principle multiple categories apply, e.g. AB Aur clearly still interacts with the large scale cloud environment, but does also show multiple spiral arms or HD 100453 has an outer companion but is also a prime example for a symmetric double-armed spiral disk. Without the ability to disentangle driving mechanisms such a categorization by appearance will always contain a certain amount of subjectivity.

ion as in the SR24 and UX Tau systems (e.g., *Mayama et al. 2020; Ménard et al. 2020*), possibly resulting of a recent fly-by event. We note that the classification proposed in Figure 9 is not absolute, and that several systems may fit in multiple categories. We attempted to classify based on the most prominent features, e.g. AB Aur shows large scale interaction with the surrounding cloud and is cited as candidate for possible late material infall by *Dullemond et al. (2019)*, however it also clearly shows multiple spiral features and could thus also be categorized as multi-armed spiral disk.

Recently, *Ren et al. (2020)* discussed that multi-epoch imaging can be used to discern small proper motions in spiral arms. Different physical causes for spirals and blobs make clear predictions for the proper motions, since some structures might have a ‘pattern’ speed that is lower than the orbital timescale. For instance, *Ren et al. (2020)* detect a small rotation ( $\sim 0.22^\circ/\text{yr}$ ) of the MWC 758 spiral

pattern, slower than the local Keplerian motion expected if spiral structure derived from gravitational instability; instead, a perturber located in the outer disk is hypothesized. Similarly, slight spiral motion reported by *Xie et al. (2021)* for HD135344B point towards external perturbers. We are only just beginning to accumulate results from proper motion studies and we can expect a rapid expansion as the time base between epochs continues to increase.

Similarly to the rings, only a handful of disks show a clear correspondence between spirals observed in the IR and in the millimeter continuum, indicating the complexity of disk evolution processes (*Dong et al. 2018; Brown-Sevilla et al. 2021*). For example, AB Aur shows large scale multiple spiral arms in scattered light (*Fukagawa et al. 2004; Hashimoto et al. 2011; Boccaletti et al. 2020a*) and, in contrast, a ring in the sub-millimeter continuum (*Tang et al. 2017*). Another case is presented in Figure 8. HD135344B

shows two spiral arms in the IR (e.g., *Muto et al.* 2012), while in the sub-millimeter regime, presents a ring with an additional azimuthal asymmetry at larger radii (*van der Marel et al.* 2016; *Cazzoletti et al.* 2018). Such a correspondence is often observed (*Garufi et al.* 2018; *van der Marel et al.* 2021). While joint analysis of high resolution images at both wavelengths has only been done in a handful of cases (*Dong et al.* 2018; *Baruteau et al.* 2019), it has the potential to constrain the possible location of the planet/companion, the 3D structure of the disk and in particular, its vertical thermal structure. *Rosotti et al.* (2020) compared the morphology of spirals of HD100453 observed with SPHERE and ALMA, and found that the opening angles of the spirals in the surface layers is much larger than in the midplane tracer. As the opening angle is directly related to the sound speed, and hence to the disk temperature, *Rosotti et al.* (2020) interpreted this as a clear evidence for a vertical thermal stratification.

## 5.2. Azimuthal shadows & misaligned inner disks

Shadows are another recurrent feature of disk images in scattered light. While in principle any region of low surface brightness seen in polarimetric maps can be due to shadows, the community widely names shadows only those dips in the disk brightness confined to specific azimuthal angles. Here we refer to these structures as azimuthal shadows. The prototypical example of such features is the two intensity drops seen to north and south in the disk of HD142527 (*Canovas et al.* 2013; *Avenhaus et al.* 2014b, see Figure 10). Through radiative transfer modeling, *Marino et al.* (2015) interpreted these regions as shadows cast by a significantly misaligned portion of the inner disk. Such a disk component was possibly imaged by *Avenhaus et al.* (2017) as close as 4 au from the star. In general, azimuthal shadows with a diverse morphology were revealed in several disks, as we review in this section and show in Figure 10. These features offer the possibility to indirectly map the inner disk geometry and its temporal evolution since marked changes in the scattered light emission on months to years times scales can be caused by shadowing from the inner disk with its shorter dynamical timescales. Further, distinctive shadow patterns tell us about the inner disk geometry on sub-au physical scales typically only accessible by long-baseline IR interferometry.

Two main classes of azimuthal shadows are recurrently observed, that are narrow shadows of a few degrees in azimuthal extent that are often seen as two symmetric narrow lanes, and broad shadows where up to half a disk is faint (see Figure 1 and Figure 10). A particularly clear example of narrow shadow can be found in SU Aur. In Figure 11, the outer disk and envelope are illuminated in scattered light (*Ginski et al.* 2021b). Near the central star, a dark lane can be seen suggesting a shadow cast by a physically-thin disk that is very misaligned with the outer disk. Indeed, in this rare case an near-IR interferometry image on 1000× smaller scales was obtained using the

CHARA Array (*Labdon et al.* 2019) confirming this hypothesis. In the case of SU Aur, it is possible that such a misalignment is caused by late-time interactions with infalling material (e.g., *Dullemond et al.* 2019). Other notable examples of narrow shadows include GG Tau A (*Krist et al.* 2002; *Itoh et al.* 2002, 2014; *Keppler et al.* 2020b) – where the shadows are due to the material in the surrounding of the binary system, RX J1604.3-2130 (*Pinilla et al.* 2015, 2018) and HD135344B (*Garufi et al.* 2013; *Stolker et al.* 2017b) – where the dips are highly variable in both morphology and position, HD100453 (*Wagner et al.* 2015; *Benisty et al.* 2017) – where shadows appear morphologically connected with the spiral arms, and DoAr44 (*Avenhaus et al.* 2018) – where the shadows have a radio counterpart (*Casassus et al.* 2018). Recently, *Bohn et al.* (2021) analyzed a sample of 20 transition disks around T Tauri and Herbig AeBe stars, observed with VLT/GRAVITY and ALMA to search for evidence for misalignments between the inner and outer disk regions. They found that six disks exhibit significant misalignments, among which three disks (HD100453, HD142527 and CQ Tau) show shadows in scattered light images, with locations that match well the predictions from the inner/outer disk geometry derived with VLT/ALMA respectively. For three other disks that are found significantly misaligned (V1247 Ori, V1366 Ori, and RY Lup), there is no evident sign of shadows in the scattered light images. On the other hand, the shadows observed in DoAr44, HD135344 B, and HD139614 while consistent with misalignments show a complex morphology that can not be well described with a simple misaligned inner disk.

In general, when there is smaller misalignment, an inner disk will cast a broader, less distinctive, shadow. HST/STIS (*Debes et al.* 2017) found a moving shadow pattern around TW Hya, with a timescale suggesting an precessing inner disk (possibly driven by a close-in exoplanet). *Benisty et al.* (2018) found a dramatic contrast between the disk surface brightness on the east compared to west side of HD 1430006 that can be modelled by an inner disk misaligned by 30°. As explained in Section 3, an inner massive exoplanet on a slightly inclined orbit can sufficiently misalign the inner disk and cast similar wide-angle shadows (*Nealon et al.* 2019; *Ballabio et al.* 2021). At first glance, HD 139614 appears to be another case of a nearly-aligned inner disk casting a wide-angle shadow (*Muro-Arena et al.* 2020; *Laws et al.* 2020), but the shadow is *too wide* and *Muro-Arena et al.* (2020) argue for the existence of two distinct warped or misaligned regions. Note that even when the inner disk is mostly aligned, there can be more subtle shadowing effects such as the reddening of starlight (not full shadowing) by inner dust rings that partially occlude the outer disk (e.g., HD169142; *Monnier et al.* 2017).

Not all shadow patterns are caused by misaligned disks. Even within the misaligned-disk paradigm, many workers (e.g., *Stolker et al.* 2017b; *Pinilla et al.* 2018) noted additional shadow variability requiring scale-height (H/r) variation in the inner disk atmosphere that could be due to irregular clumps or dust lifted at the base of magnetospheric ac-



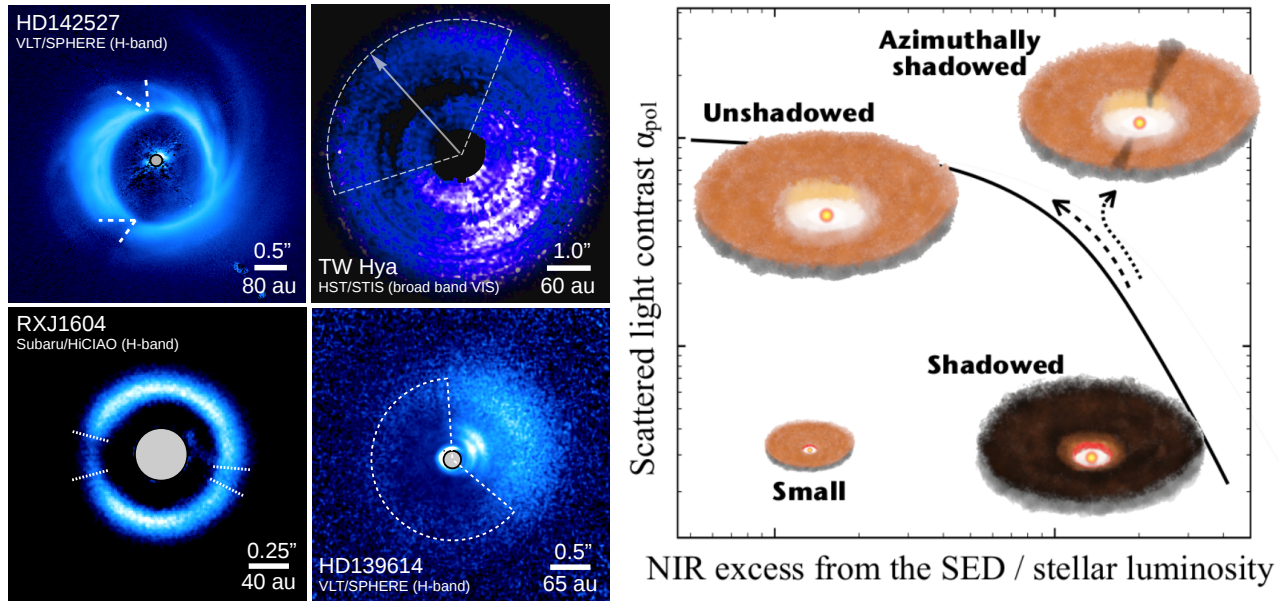


Fig. 10.— Shadows in disks. **Left:** Four exemplary cases of azimuthal shadows detected in disks with different facilities. The disks around HD 142527 (*Hunziker et al. 2021*) and RX J1604 (*Mayama et al. 2012*) show narrow shadows, indicative of a strong misalignment of inner and outer disk. TW Hya (*Debes et al. 2017*, image credit: ESA) and HD 139614 (*Muro-Arena et al. 2020*) show broad shadows, indicative of a small misalignment or warp in the disk. **Right:** Sketch illustrating the interplay between inner and outer disk, observed as an anti-correlation between the disk brightness in scattered light and the near-IR excess (black solid line, see *Garufi et al. 2022*).

cretion columns. HD 163296 shows globally variable scattered light emission (*Rich et al. 2019, 2020*) but we know the inner and outer disks are well aligned (*Monnier et al. 2017; Setterholm et al. 2018*). *Rich et al. (2019)* suggests obscuration by dust clouds elevated in a disk wind might be at play while recent VLT/MATISSE and VLT/GRAVITY interferometric observations of the HD 163296 reveals an inner disk asymmetry possibly caused by a vortex (*Varga et al. 2021; Gravity Collaboration et al. 2021*). There is a likely a close connection between these shadowing mechanisms to the well-studied photometric “dipper” phenomena (e.g., *Cody et al. 2014; Bodman et al. 2017*) where young stars show diverse light curves due to variable obscuration by intermediate and high inclination close-in disks. The causes for such variations in scale height could include magnetic field interactions (*Bouvier et al. 1999*).

Supporting this general picture, *Garufi et al. (2018)* discussed an empirical correlation between disks with narrow shadows and anomalously high thermal near-IR excess from the SED, possibly indicating a dynamically perturbed inner disk. Following up on this finding, *Garufi et al. (2022)* found that, excluding these radially shadowed disks, large disks present an anti-correlation between the disk brightness in scattered light and the near-IR excess. Therefore, a final picture is emerging for the inner/outer disk interplay as is drawn in the sketch of Figure 10 (right panel), with the inner disk geometry determining the illumination pattern in the outer disk. On the one hand, uniformly shadowed disks (see Sect. 4.1) may in principle evolve as unshadowed disks as the material in the inner disk is depleted or as the

inner disk vertical structure changes. On the other hand, radially shadowed disk may represent a particular stellar-companion-disk configuration that leads to an inner disk geometry that yields both an exceptionally high thermal near-IR excess and azimuthally confined shadows.

Time variability of the shadow patterns themselves require either precession of the inner disk with respect to the outer disk, or orbital evolution of inner disk warps or height structure in the inner disk wall. While inner disk precession is likely slow ( $\gg$  orbital time), Keplerian rotation of warps or inner disk structures will cast long shadows that can change on months timescale. Note that the changing shadowing also changes the temperatures in the upper layers and *Espaillet et al. (2011)* reported “see-saw” changes in IR SEDs of T Tauri disks using Spitzer, observing increased near-IR flux (e.g., higher scale height of inner disk) associated with decreased mid-IR flux (more shadowing by inner disk). The variability of the shadows position and contrasts observed in RX J1604.3-2130 was found to be within timescales of less than a day (*Pinilla et al. 2015*). This implies that the dust casting the shadow is located very close to the star (0.06 au, at corotation radius), in an irregular misaligned inner disk, which dust content is accreted/replenished by accretion in very short timescales (*Sicilia-Aguilar et al. 2020*). In contrast, the shadow detected in TW Hya was measured to move at a constant angular velocity of  $22.7^\circ \text{yr}^{-1}$  in a counterclockwise direction, corresponding to a period of 15.9 yr assuming circular motion (*Debes et al. 2017*). The sample of disks for which the temporal evolution of shadow features is being systemati-

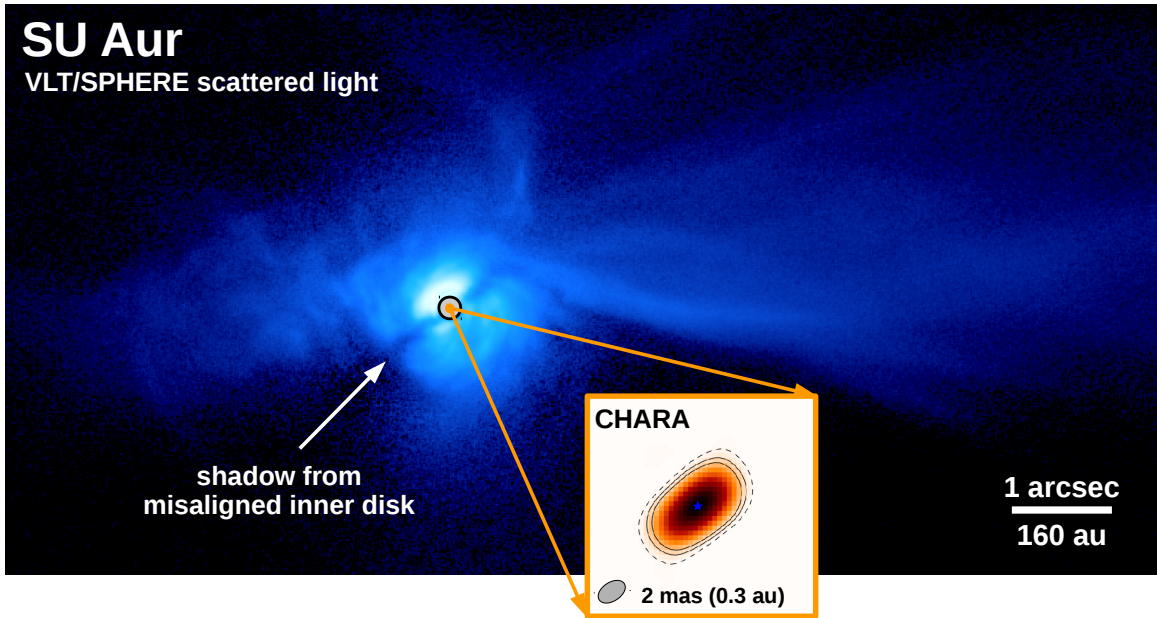


Fig. 11.— Misaligned disk system in SU Aurigae. A complex scattered-light disk is seen on large scales (VLT/SPHERE; *Ginski et al. 2021b*) with a dark lane caused by shadowing from a misaligned inner disk that has been directly imaged with the CHARA Array (*Labdon et al. 2019*). The inset box is zoomed by a factor of  $\sim 1000\times$ .

cally tracked is still small, with currently only four cases in the literature. Two of them are the aforementioned cases of TW Hya as well as RX J1604.3-2130. In addition this was also done in the cases of HD 135344B (*Stolker et al. 2017b*) and PDS 66 (*Schneider et al. 2014; Wolff et al. 2016*). The shortest monitoring time scales vary between days for RX J1604.3-2130, weeks for HD 135344B, months for PDS 66 and years for TW Hya.

### 5.3. Demography of disk substructures

At time of writing, nearly 130 stars hosting a planet-forming disk have polarimetric observations published. Out of these, the disk is firmly resolved around approximately 80 targets, with the remaining 50 equally distributed between non-detections and detection of scattered light from the environment. From the 80 detected disks, substructures are detected in 45 objects. For the remaining 35 disks, the absence of substructure can be explained by the small disk extent (e.g., ET Cha, *Ginski et al. 2020*), the faint signal in scattered light (e.g., CI Tau, *Garufi et al. 2022*, see Sect. 4.1), or the very inclined geometry of the disk (e.g., T Cha, *Pohl et al. 2017*). Therefore, the current census indicates that disk substructures are ubiquitous when the disk is bright and extended enough.

A demographical study of disk substructures in scattered light was carried out by *Garufi et al. (2018)*, who considered the 58 targets available at that time. All targets were classified in six main categories: disks hosting multiple rings, one or two bright spirals on small scale, multiple gigantic spirals on large scale, a unique bright rim, as well as faint and small disks.

At present, we can extend this type of study to a total sample of 76 objects excluding the aforementioned inclined disks and sources dominated by ambient emission. From our count, spiral arms are currently detected in 16 disks (6 giant disks with multiple arms at large scale and 10 smaller disks with 1-2 bright spirals at small scale), multiple rings in 18 disks, and bright rim at the outer cavity edge in only 3 disks. In Figure 12, the distribution of the various classes of disks with three meaningful stellar and disk properties reveals trends in line with the results of *Garufi et al. (2018)*.

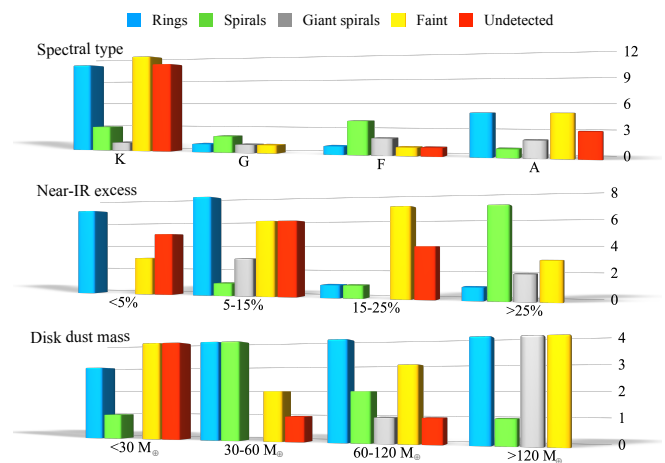


Fig. 12.— Distribution of targets with ring-, spiral-, giant spiral-, faint, and undetected disks with spectral type (top), near-IR excess (middle), and disk dust mass (bottom).

*Spiral disks.* Spirals are predominantly found around early-type stars. The recent discovery of spirals in the disk of WW Cha (*Garufi et al.* 2020) and GQ Lup (*van Holstein et al.* 2021) slightly changed this view. However, their formation is – unlike those of isolated early-type stars – probably due to the interaction with the accreting material and the stellar companion, respectively. The paucity of spiral-disks around late-type stars can in principle be explained by their low luminosity, and therefore by the low disk temperature because the detectability of spirals increases with the pitch angle which in turn is correlated with the aspect ratio and therefore temperature (*van der Marel et al.* 2021), or alternatively by their low mass and young age. Disks with 1–2 spirals on small scale (tens of au) are not particularly massive whereas those with multiple spirals at large radii (hundreds of au) are. This suggests a possible different origin for these two classes of spirals. The origin of spirals may be intimately related to the structure of the inner disk since the near-IR excess from the SED of these spiral-hosting targets is significantly higher than that of ring-hosting targets.

*Ring disks.* Targets with ring disks are uniformly distributed across stellar properties and disk mass. However, the vast majority of disks with rings is found in sources with low near-IR excess. In this regard, disks with rings and spirals therefore show a dichotomic behavior.

*Faint and undetected disks.* A very large number of targets with faint or no detection in scattered light is found around T Tauri stars. However, this behavior is not dictated by their low luminosity (*Garufi et al.* 2022). Instead, it is likely due to the young age of these sources. In fact, low-mass stars that are older than 3–5 Myr are currently not observed (see Figure 3) while the disk around intermediate-mass stars older than that can only persist if disk substructures such as an inner cavity is present, and this determines their brightness in scattered light (see Sect. 4.1). Undetected disks are mostly those with low mass (since small) while several faint disks are found among those with high mass (since self-shadowed).

*Shadows.* The distribution of shadows with the spectral type is uniform from K to F types. However, none have been found around stars earlier than A9. As commented in Sect. 5.2, shadows are – similarly to spirals – primarily associated with a high near-IR excess from the SED. This is particularly true for narrow shadows, as five of seven targets with such features sit in the upper quartile shown in Figure 12. So far, this empirical correlation is poorly explained by modeling effort but it clearly reinforces the connection between the morphology of shadows and that of inner environment around the star.

## 6. Direct imaging of planets

High-angular resolution observations at near-IR and optical wavelengths are not only excellent tools to probe the properties of protoplanetary disks, but are also used to directly search for substructure-inciting planets within disks (see details in Chapter 22 by *Currie et al.* on direct imaging

and spectroscopy of extrasolar planets).

Young, giant planets are still radiating remnant energy from the formation process, and direct near-IR thermal emission is one way to detect them (see Section 6.2). The relative contributions of direct photospheric emission and emission from circumplanetary material to the thermal emission from protoplanets is a subject of debate, and there is both observational (*Stolker et al.* 2020; *Wang et al.* 2021) and theoretical (*Zhu* 2015; *Szulágyi et al.* 2019a; *Szulágyi and Garufi* 2021) support for substantial contribution from circumplanetary disks (CPDs). As the degree of CPD contamination of thermal emission from protoplanets is not well constrained, protoplanet mass estimates from evolutionary models carry a high degree of uncertainty.

Additionally, some transition disk host stars have accretion rates high enough to require the transport of gas from the outer disk (*Manara et al.* 2014), through their cleared central cavities, and onto the star. Whether accretion onto the primary stars happens via high velocity low optical depth flows (e.g. *Rosenfeld et al.* 2014) or dense high-optical depth streamers (e.g. *Casassus et al.* 2013) remains a subject of debate, but either mechanism results in similar predictions of persistent accretion onto any protoplanets embedded inside transitional disk cavities. This has prompted several searches for accreting protoplanets in planet-forming disks (see Section 6.3; *Zurlo et al.* 2020; *Cugno et al.* 2019). Accretion shocks caused by infalling gas on the planet itself or on the surface of the circumplanetary disk will give rise to both excess UV continuum emission from the stellar hotspot and line emission from infalling gas, making star-to-planet contrast ratios more favorable at a range of wavelengths where substantial accretion luminosity is present (see section 6.3).

PDS 70b’s detection in multiband thermal emission (e.g. *Keppler et al.* 2018) as well as in H $\alpha$  (e.g. *Wagner et al.* 2018; *Haffert et al.* 2019) and the lack of any potentially confounding nearby dust structures made it the first uncontroversial direct detection of an accreting protoplanet, as detailed in Section 6.1. The successful operation of ALMA’s longest baseline modes has enabled two complementary approaches to direct protoplanet detection. The first technique is to search for circumplanetary material, analogous to the disk hypothesized to exist around Jupiter in the protosolar nebula (*Batygin and Morbidelli* 2013, 2020). This has been successfully applied in the case of PDS 70 c (*Isella et al.* 2019; *Benisty et al.* 2021), and the DSHARP survey (*Andrews et al.* 2018) has also provided detection limits for CPDs in many observed mm gaps (*Andrews et al.* 2021). The second method used for protoplanet study with ALMA is to search for kinematic signatures in mm gas emission, indicative of departure from Keplerian rotation due to an embedded planet (as detailed in section 6.4).

### 6.1. Protoplanets in the PDS70 system

As the most robustly confirmed case to date, the PDS 70 system is an ideal laboratory to observationally study plan-



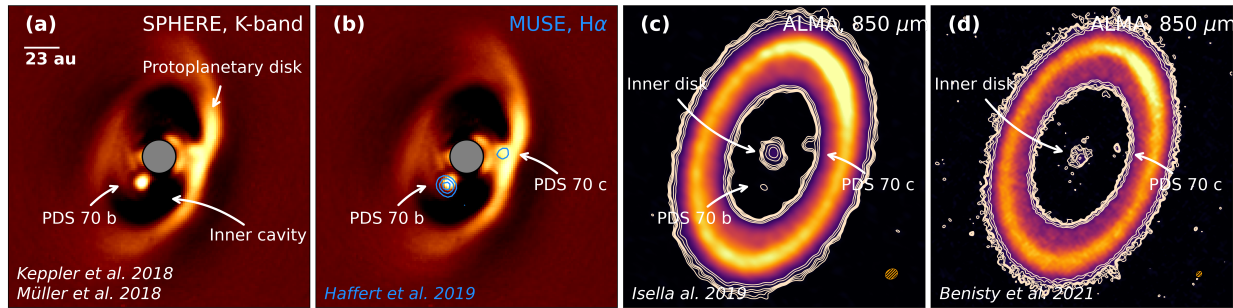


Fig. 13.— The PDS 70 system as seen with SPHERE in the near-IR (left), overplotted with blue contours from H $\alpha$  observations (center left), and as observed in the sub-millimeter continuum (middle right, right). The difference between panels (c) and (d) is the angular resolution of the data, the beam is provided in orange color in the bottom right corner. The SPHERE K-band data and the MUSE H $\alpha$  data both have an effective resolution of 70 mas, i.e. a factor  $\sim 3$  worse than the ALMA data shown in panel (d).

etary system formation. At a distance of 112.4 pc (*Gaia Collaboration et al. 2020*) and with an age of  $\sim 5$  Myr (*Müller et al. 2018a*), PDS 70 is a young T Tauri star surrounded by a protoplanetary disk. The system has long been suspected to host forming planets based on its large observed central cavity ( $0''.43$ , *Long et al. 2018; Dong et al. 2012b; Hashimoto et al. 2012, 2015*). Multi-epoch near-IR observations using the VLT/SPHERE instrument (*Beuzit et al. 2019*) as part of the SHINE exoplanet survey (*Chauvin et al. 2017*) revealed a point source, PDS 70 b, at a projected separation of  $\sim 200$  mas and a position angle of  $\sim 150^\circ$  (see Figure 13, left; *Kepler et al. 2018; Müller et al. 2018a*). The planet was subsequently confirmed through the detection of accretion excess emission in the H $\alpha$  line and in UV continuum (*Wagner et al. 2018; Haffert et al. 2019; Hashimoto et al. 2020; Zhou et al. 2021*). H $\alpha$  imaging by *Haffert et al. (2019)* revealed a second accreting planet in the system, PDS 70 c, located at a projected separation of  $\sim 230$  mas and a position angle of  $\sim 270^\circ$  (see Figure 13, center panel). While extraction of signal from PDS 70 b benefits from its location well within the gap of the disk, excluding any possible confusion with disk features, PDS 70 c's emission is more challenging to disentangle from the disk due to its close projected separation from the inner edge of the outer disk (*Mesa et al. 2019a; Stolker et al. 2020; Wang et al. 2020*).

Current astrometric measurements of the PDS 70 planets span a baseline of more than 7 years. Orbital fits to the astrometry place PDS 70 b on a slightly eccentric ( $\epsilon \sim 0.2$ ) orbit, while the orbit of PDS 70 c is consistent with being circular (*Wang et al. 2021*). With semi-major axes of  $\sim 21$  au and  $\sim 34$  au, respectively, the planets are likely locked in a dynamically stable 2:1 mean-motion resonance (*Wang et al. 2021*), as supported by hydrodynamical simulations of the system (*Bae et al. 2019; Toci et al. 2020*).

The masses of the two planets, are still uncertain, but have been estimated using a range of approaches, all of which converge on masses that lie solidly in the planetary regime. Dynamical stability and constraints on disk ec-

centricity confer upper limits of  $\lesssim 10 M_{\text{Jup}}$  on both companions (*Wang et al. 2021; Bae et al. 2019*). Comparisons of near-IR spectro-photometry to evolutionary and atmospheric models yield masses in the range of  $\sim 1$  to  $\sim 17 M_{\text{Jup}}$  (*Kepler et al. 2018; Müller et al. 2018a; Haffert et al. 2019; Mesa et al. 2019b; Stolker et al. 2020; Wang et al. 2020*). Measured H $\alpha$  line properties suggest dynamical masses of  $\sim 12$  and  $\sim 11 M_{\text{Jup}}$  for PDS 70 b and c, respectively (*Hashimoto et al. 2020*), consistent with the range of masses derived from near-IR spectro-photometry.

PDS 70 b and c present very red and almost featureless near-IR SEDs compared to other planetary mass companions, hinting at the presence of dust at or near the planets which may originate in the planetary atmosphere, the accretion column, or in a surrounding circumplanetary disk (*Müller et al. 2018b; Christiaens et al. 2019; Stolker et al. 2020; Wang et al. 2021; Cugno et al. 2021*). Further evidence of circumplanetary dust around PDS 70 c comes from ALMA sub-millimeter continuum observations, revealing compact emission co-located with the H $\alpha$  and near-IR emission of the planet (*Isella et al. 2019; Benisty et al. 2021*). Some emission is detected close to PDS 70 b, but it appears faint and with an unclear morphology. In Figure 13, middle right, and right panels, the sub-millimeter continuum observations are presented with two different angular resolutions. At very high angular resolution (right), the emission co-located with PDS 70 c is separated from the outer disk, but the faint emission around PDS 70 b is not retrieved. The dust mass of the CPD, as inferred from these continuum observations, is on the order of  $\sim 0.01$  Earth masses, where the precise value depends on the assumed grain properties (*Benisty et al. 2021*). It is not clear whether the nature of the CPDs around PDS 70 b and PDS 70 c is the same (e.g., accretion or decretion disk) considering the fact that one is located in a very gas-depleted cavity, while the other is adjacent the main disk reservoir.

The presence of dust at or near the planets can also be inferred from optical observations. Following the theoretical models of *Aoyama et al. (2018)* and neglecting any fore-

ground extinction, the line flux ratio of  $H\beta$  to  $H\alpha$  originating from the post-shock region of the planetary atmosphere should be near unity. Considering the clear detection of  $H\alpha$  but non-detection of  $H\beta$ , *Hashimoto et al.* (2020) derived lower limits on the optical extinction of  $> 2.0$  mag and  $> 1.1$  mag for PDS 70 b and c, respectively, assuming that the post-shock region is the primary source of hydrogen line emission. This extinction is presumably caused by the presence of small, unseen dust grains coupled to the gas within the cavity.

Theoretical models predict that the presence of a massive planet in a disk generates a pressure bump outside of its orbit, trapping large dust particles and allowing small grains to flow through the cavity (*Pinilla et al.* 2012). Detailed hydrodynamical simulations by *Bae et al.* (2019) strongly suggest that PDS 70 b and c open a common cavity, trapping submillimeter particles at distances similar to the observed location of the mm continuum ring. This is supported by the fact that disk rotational velocities, as measured from  $^{12}\text{CO}$  observations with ALMA, reveal radially extended perturbations and only recover Keplerian rotation at regions close to the continuum ring (*Keppeler et al.* 2019). This indicates a peak in the radial pressure profile close to the radial accumulation of sub-mm particles, as expected for the process of particle trapping.

## 6.2. Protoplanet IR candidates

Embedded protoplanet candidates have been put forward in a number of disk systems in recent years (*Kraus and Ireland* 2012a; *Quanz et al.* 2013a; *Brittain et al.* 2013; *Biller et al.* 2014; *Reggiani et al.* 2014; *Quanz et al.* 2015a; *Sallum et al.* 2015; *Currie et al.* 2015; *Garufi et al.* 2016; *Reggiani et al.* 2018; *Wagner et al.* 2019; *Gratton et al.* 2019), but many have proven difficult to robustly verify as point-sources (*Thalmann et al.* 2016; *Rameau et al.* 2017a; *Follette et al.* 2017; *Mendigutía et al.* 2018; *Ligi et al.* 2018; *Sissa et al.* 2018; *Currie et al.* 2019). The complex morphologies of the disks in which protoplanet candidates are embedded make disentanglement of planet and disk signals complex, and the fidelity of post-processing algorithms for robust signal detection is a subject of debate. The first reported protoplanet detections was of a  $\approx 15\text{AU}$  planetary-mass companion to the star LkCa 15, LkCa 15 b, by non-redundant aperture masking (NRM) (*Kraus and Ireland* 2012b). An object consistent with the *Kraus and Ireland* (2012b) companion was detected in several additional NRM epochs, as well as directly in  $H\alpha$  emission by *Sallum et al.* (2015). The ‘b’ companion, as well as two other point sources, LkCa 15 ‘c’ and ‘d’, were reported in several additional NRM epochs (*Sallum et al.* 2016). However, the coincidence of the LkCa 15 companions with an inner disk component imaged in polarized intensity (*Thalmann et al.* 2016) and total intensity (*Currie et al.* 2019) has led to speculation that it may be due to the scattered light signal from an asymmetrically disk. In fact, the candidates LkCa 15 b,c,d, HD100546 b,c, and HD 169142 b,c

have been put forward as both protoplanets (*Kraus and Ireland* 2012b; *Sallum et al.* 2015; *Quanz et al.* 2015b; *Currie et al.* 2015; *Biller et al.* 2014) and potential disk signatures (*Thalmann et al.* 2016; *Currie et al.* 2019; *Follette et al.* 2017; *Rameau et al.* 2017b; *Pohl et al.* 2017; *Biller et al.* 2014; *Ligi et al.* 2018) in the literature. Other protoplanet candidates, such as those in MWC 758 have yet to be fully verified (e.g. *Reggiani et al.* 2018), with additional observations, to rule out a disk contribution that remains significant enough that it could lead to false detection.

Although current high-contrast imaging instrument limits for point sources are approaching contrasts of nearly  $10^{-5}$  at  $0''.1$  and  $10^{-7}$  at  $0''.5$  (see Figure 14), these levels are achievable for only a small number of bright, nearby systems. Protoplanets are both farther away ( $d \sim 150\text{--}200$  pc) and more heavily extinguished (by material local to the system and interstellar dust) than most directly imaged exoplanets ( $d \sim 50$  pc). Planet searches at longer wavelengths (e.g. *Stone et al.* 2018; *Launhardt et al.* 2020; *Jorquera et al.* 2021) are promising avenues for robustly detecting thermal emission from embedded protoplanets. Depending on the mass and age of the planet, and thus its temperature, the peak of the planet emission is located in the near or mid-IR, maximizing the photons received from the planet and at the same time minimizing the required contrast relative to the central star. Furthermore dust opacities are lower at longer wavelengths (*Ossenkopf and Henning* 1994; *Woitke et al.* 2016), allowing for an easier detection of heavily embedded planets. Simulations of the expected fluxes and a discussion of the detectability of embedded planets with surrounding circumplanetary material is given in *Szulágyi et al.* (2019b). At these longer wavelengths, angular resolution however becomes increasingly challenging. Ground based instrumentation in the L ( $3.8\mu\text{m}$ ) and M-bands ( $4.78\mu\text{m}$ ), is limited to planets outside of  $\sim 125$  mas, which translates into  $\sim 20$  au for the nearby star forming regions. Mid-IR ( $\sim 10\mu\text{m}$ ) observations by the James Webb Space Telescope will only have an angular resolution of 425 mas. This limits searches for embedded planets to the most extended disks at these wavelengths. Under the assumption that the substructures observed in disks are due to planets, a putative underlying population of protoplanets could be inferred, as has been done at longer wavelengths (*Zhang et al.* 2018; *Lodato et al.* 2019). Using analytical prescriptions for the gap properties, *Asensio-Torres et al.* (2021) derived the expected planet masses for a number of features in disks observed with SPHERE and compared those to the detection limits under various evolutionary models. The results are shown in Figure 15, extracted from *Asensio-Torres et al.* (2021). We note that this approach, while insightful, remains model-dependent, in particular on the assumptions on the disk properties (viscosity, temperature structure).

## 6.3. Search for accretion tracers

Disambiguation of protoplanets from ambient circumstellar disk structures requires clear separation from disk

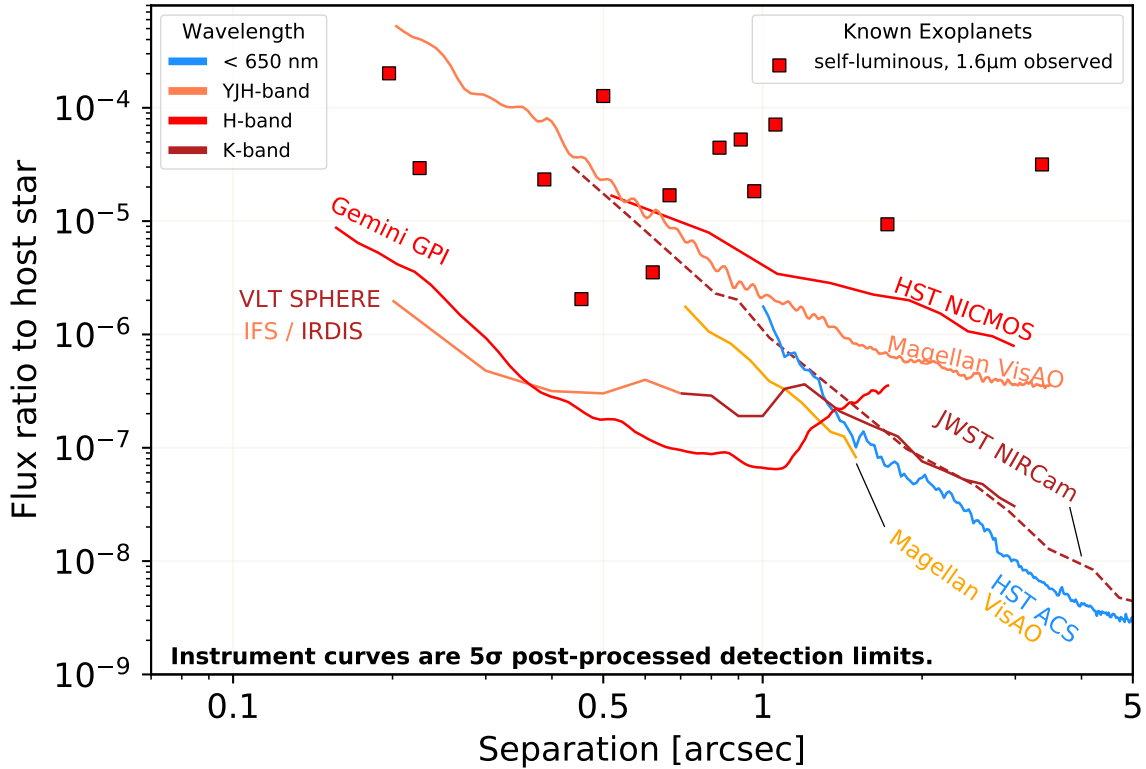


Fig. 14.— Contrast curves at optical and near IR wavelengths from a selection of ground and spaced based high-contrast imaging instruments. The curves depict  $5\sigma$  post-processed contrast limits, and are color coded by wavelength of observation. The points depict the H-band contrasts of directly-imaged companions. Though the post-processing techniques and exposure times are inhomogeneous, the datasets used to derive them are all exemplary, representing an approximation of the ‘best’ achievable contrasts with each instrument. Image Credit: Vanessa Bailey (<https://github.com/nasavbailey/DI-flux-ratio-plot>) Sources: STIS handbook; E. Choquet, J. Krist, B. Macintosh, personal communication; *Beichman et al. (2010)*; *Vigan et al. (2015)*

material (as in PDS 70 b), detection of orbital motion, or emission that is inconsistent with circumstellar disk emission, such as accretion signatures. Excess emission from accreting objects is typically thought to consist of: (a) continuum emission from an accretion “hot spot” peaking in the NUV–optical range, (b) excess line emission (primarily Hydrogen) from infalling or shocked gas at a range of wavelengths, and (b) excess near-IR emission from the warm accretion disk (e.g. *Hartmann et al. 2016*; *Zhu 2015*).

**Continuum excess** in the blue optical to ultraviolet has been successfully detected for several bound brown dwarfs and even one protoplanet, PDS 70 b, with HST (*Zhou et al. 2014, 2021*). Low-resolution spectroscopy and spectrophotometry of these sources yields important constraints on continuum emission from the accretion hotspot. These studies are limited to the widest companions because of the small aperture and relatively limited options for PSF subtraction with HST. Near-IR continuum emission has also been detected from several protoplanets (notably PDS70 b and c, *Kepler et al. 2018*; *Müller et al. 2018b*), and protoplanet candidates, including at very tight separation with

interferometric techniques (e.g., *Sallum et al. 2015*; *Biller et al. 2014*). Some attempts have been made to quantify the contribution of the circumplanetary accretion disk to emission from protoplanets at these wavelengths (e.g., *Zhu 2015*; *Eisner 2015*), however uncertainties in accretion disk structure and disk and planetary physical properties make disentangling planetary photospheric and accretion disk contributions difficult.

$H\alpha$  is among the brightest accretion emission lines, and computational models suggest that planet/star contrasts at  $H\alpha$  should be several orders of magnitude more favorable than thermal emission in the near-IR (*Mordasini et al. 2017*). This allows  $H\alpha$  excess to be detected from the ground, where larger telescope apertures combined with shorter wavelength emission allows for detection of accretion from more tightly-separated companions. Achievable contrasts at  $H\alpha$  inside of transitional disk cavities are typically  $\approx 10^{-3} - 10^{-2}$ , where only the most massive and/or strongly accreting planets are expected to be detectable with current technology (*Mordasini et al. 2017*), and this detection requires aggressive PSF subtraction.

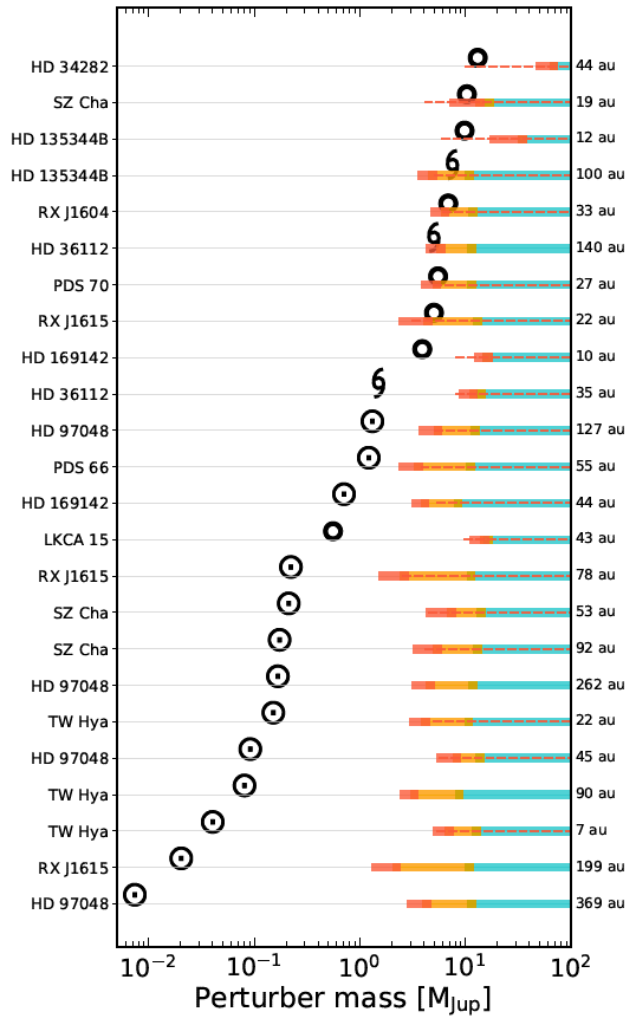


Fig. 15.—  $5\text{-}\sigma$  detection limits compared to planets masses expected from modeling of the substructures. The masses are estimated using the AMES-DUSTY, BEXHOT and BEX-WARM initial starts models (red, orange, blue, respectively). The locations of the substructures for each star are given on the right. From *Asensio-Torres et al. (2021)*.

Despite the technical complexities, successful detections of accreting protoplanets have allowed for estimation of planetary accretion rates, an important constraint on their evolution, ultimate mass, and perhaps even informing their formation mechanism (e.g., *Stamatellos and Herczeg 2015*). Initial estimates of accretion rates for protoplanets have been high, comparable to those of T Tauri stars ( $\sim 10^{-11} - 10^{-9} M_{\odot}/\text{yr}$ ). These estimates should be interpreted as very rough approximations, as calibration of accretion signatures remains difficult. At present, it is unclear to what extent the magnetospheric accretion paradigm for higher mass objects holds at planetary masses.

Conversion of an accreting object’s luminosity or contrast at a single accretion-tracing wavelength to a mass accretion rate estimate relies on a number of factors. Key among these are (a) an assumption of a scaling relation be-

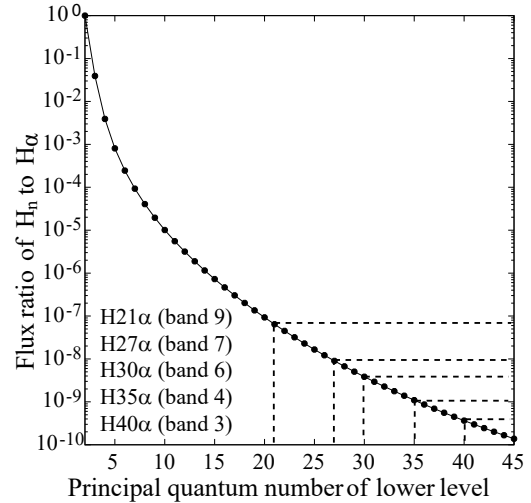


Fig. 16.— Predictions for intensity ratios of  $\text{H}_n\alpha$  to  $\text{H}\alpha$  calculated via the one-dimensional radiative hydrodynamic models of *Aoyama et al. (2018)*.

tween the luminosity at the observed wavelength (e.g.,  $\text{H}\alpha$ ) and the total accretion luminosity at all wavelengths, and (b) the companion’s physical properties, including mass and radius. For classical T-Tauri stars, scaling relations have been established empirically through a range of multiwavelength observations (e.g., *Rigliaco et al. 2012; Alcalá et al. 2017*), however it is unclear to what extent these relations hold at lower masses. Poor understanding of magnetic field strengths and geometries for protoplanets make it difficult to infer the precise accretion mechanism (e.g., magnetospheric accretion via a column of infalling gas or more diffuse boundary layer accretion). Furthermore, while accretion line emission for T Tauri stars is believed to originate primarily in the infalling accretion column, the lower temperatures in a protoplanetary atmosphere are predicted to make the post-shock region the dominant source of Hydrogen line emission from protoplanets (*Aoyama et al. 2018, 2020*). The very different physical properties in this region may dramatically alter line-to-total accretion luminosity relations for lower mass objects. Planetary masses and radii are also much more poorly constrained, observationally and theoretically, compared to stars, yielding large uncertainties in mass accretion rate estimates.

Though properties of gaps, such as width and degree of depletion, have been used to predict planetary masses (e.g., *Bae et al. 2018; Zhang et al. 2018; Lodato et al. 2019*), they do not provide unique constraints due to the degeneracies of planet mass with disk viscosity and aspect ratio (*Fung et al. 2014*). Since meridional flow in planetary gaps is predicted to be supersonic, accreting gas shocks in the planetary or circumplanetary disk atmosphere. When the velocity of accreting gas is high (more than  $\sim 30$  km/s; *Aoyama et al. 2018*), shocks cause the gas temperature to be high enough ( $\gtrsim 10^4$  K) to ionize atomic hydrogen, leading to line emission. Hydrogen radio recombination lines (HRRL) for the

higher principal quantum number levels ( $n \gtrsim 20$ ) might be a good kinematic tracer of accreting protoplanets. At radio wavelengths, dust extinction in the protoplanetary disk is negligible compared to  $H\alpha$ , especially in the optically thin gap region of the disk. If detected, mm Hydrogen line ratios will allow for estimation of planetary masses, given assumptions about planetary radii and free fall velocities, by applying radiation-hydrodynamic models of the shock-heated accretion flow (Aoyama et al. 2018).

#### 6.4. Kinematic detections of protoplanets

The velocity structure of disk gas as revealed by ALMA provides a unique, indirect signature of protoplanets (see Chapter by Pinte et al.). A massive planet embedded in the gas disk is expected to cause a local deviation from Keplerian velocity field (e.g., Perez et al. 2015), with a characteristic pattern of sub- and super-Keplerian velocities near the planetary perturber as a result of the lower gas pressure at the location of the planetary clearing (e.g., Kley et al. 2001; Tanigawa et al. 2012). This can be traced in the gas velocity channels as seen in Figure 8 (right; so-called velocity kinks) and also as a doppler-flip signature (Casassus and Pérez 2019) in velocity maps. Recently, Izquierdo et al. (2021b) proposed a statistical method to identify and quantify kinematical perturbations and considered the contributions from both the upper and lower emitting disk surfaces. This framework was validated with observational data on HD163296 (Izquierdo et al. 2021a).

These deviations depend on the planet masses, and can be used to estimate the unseen planet mass by comparing with hydrodynamic simulations. To date roughly ten objects have been reported to possess the so-called velocity kink structures, although some are tentative detections at low signal-to-noise ratio. Table 1 summarizes their properties, corresponding planet mass estimates, and limits on planet masses at those locations from near-IR imagery.

Another promising kinematic detection method for protoplanets would be the presence of a ‘meridional flow’. The gas flows from the disk onto the planet through the pole and produces a 3D velocity signature that could be clearly mapped in HD163296 (Teague et al. 2019) and HD169142 (Yu et al. 2021). Hydrodynamic simulations also predict a kinematic signature for circumplanetary disks in the form of a point source in the velocity channel maps (Perez et al. 2015). A tentative detection of such a point source was reported for PDS 70, using ALMA observations of the  $^{12}\text{CO}$  (3–2) line, in Keppler et al. (2019).

## 7. Future prospects

### 7.1. Perspectives

As mentioned before, multi-wavelength observations trace different vertical layers in the disk: optical/near-IR wavelengths trace small grains in the upper surface layer, while (sub-)millimeter wavelengths trace larger pebbles located at deeper layers within the disk, closer to the disk midplane. One of remaining questions of our field con-

Table 1: Planet mass estimation from ALMA kinks compared to near-IR detection limit

Object	Radial location (au)	Expected mass ( $M_{\text{Jup}}$ )	Detection limit ( $M_{\text{Jup}}$ )	Refs
HD 163296	260	2	2	1,2
	68	1–3	5	3,2
DoAr 25	60	1–3	5	3,4
IM Lup	110	1–3	2	3,5
Elias 2–27	37	1–3	20	3,5
GW Lup	61	1–3	4	3,6
HD 143006	23	1–3	>20	3,6
Sz 129	47	1–3	>20	3,6
WaOph 6	63	1–3	3	3,6
HD 97048	130	2–3	2	7,8
HD 100546	26	5–10	>20	9

References for respectively kink’s radial locations, expected planet masses, and detection limit at the kink’s locations: (1) Pinte et al. (2018), (2) Guidi et al. (2018), (3) Pinte et al. (2020), (4) Uyama et al. (2017), (5) Launhardt et al. (2020), (6) Jorquera et al. (2021), (7) Pinte et al. (2019), (8) Ginski et al. (2016), (9) Pérez et al. (2020).

cerns the connection between the observed structures in these wavelengths. Some objects exhibit very different sub-structures in different wavelengths as showed in Figure 8 (e.g., AB Aur in Fukagawa et al. 2004; Tang et al. 2017; SAO 206462 in Muto et al. 2012; Cazzoletti et al. 2018). The ALMA gas observations trace the optical depth  $\tau \sim 1$  layer that corresponds to the gas isotope abundances (e.g.,  $^{12}\text{CO}/^{13}\text{CO}=67$ ,  $^{12}\text{CO}/\text{C}^{18}\text{O}=444$ ,  $\text{C}^{18}\text{O}/\text{C}^{17}\text{O}=3.8$ , Qi et al. 2011), with less abundant gases such as  $\text{C}^{17}\text{O}$  tracing deeper disk layers. Multi-wavelength observations combined with radiative transfer modeling, could serve as building 3D structures of the disk and help understanding of possible common origin of different substructures in different wavelengths.

Near-IR observations of the polarization fraction in linear polarization could reveal the dust porosity in the disk. Since planets are thought to form via collisional aggregation of dust grains (e.g., Weidenschilling and Cuzzi 1993; Dominik et al. 2007), overcoming bouncing barrier (e.g., Wada et al. 2011) and radial drift barrier (e.g., Okuzumi et al. 2012) is an important step in grain growth. Dust porosity could be crucial to overcome these barriers. Numerical simulations by Tazaki et al. (2019) suggest that high polarization fraction ( $\sim 65\text{--}75\%$ ) in linear polarization is attributed to highly porous dust aggregates, while more compact dust structure tends to show low polarization fraction ( $\sim 30\%$ ). In observed near-IR polarization fractions, both of high ( $\sim 50\%$ ) polarization fraction (e.g., Silber et al. 2000; Perrin et al. 2009; Tani et al. 2012; Poteet et al. 2018) and



low ( $\sim 30\%$ ) one (e.g., *Canovas et al.* 2013; *Avenhaus et al.* 2014b) have been reported in literature. Thus, some of these observations may suggest the presence of large porous aggregates. Future ExAO observations of polarization fraction would provide more reliable results.

In addition, optical/near-IR circular polarization observations of protoplanetary disks might provide useful information of magnetic fields. Magnetic fields are thought to play an important role in the disk evolution via magnetically driven disk winds (e.g., *Suzuki and Inutsuka* 2009; *Suzuki et al.* 2016). The spatial distribution of close-in super-Earths is attributed to the suppression of rapid inward migration (i.e., type I migration) by magnetically driven disk winds (*Ogihara et al.* 2018), and thus, observations of the magnetic field strength and structure would be valuable to understand formation of close-in super-Earths. Circular polarization has been observed in circumstellar materials around young stars (e.g., *Fukue et al.* 2010; *Kwon et al.* 2013, 2014, 2016a,b, 2018), and has been interpreted as a result of scattering from aligned non-spherical dust grains (e.g., *Gledhill and McCall* 2000; *Wolf et al.* 2002) and the dichroic extinction (e.g., *Lucas et al.* 2005). Non-spherical dust grains could be aligned with the local magnetic field (e.g., *Davis and Greenstein* 1951; *Dolginov and Mitrofanov* 1976; *Draine and Weingartner* 1996, 1997; *Andersson et al.* 2015). *Tazaki et al.* (2017) expect that circular polarization in protoplanetary disks can be produced by scattering from aligned dust grains. Future observations of circular polarization with VLT/SPHERE and Subaru/SCEAO would constrain not only dust properties (i.e., spherical or non-spherical) but also the magnetic field in disks.

The advances in instrumentation in the last decade have led to a high temporal stability of ground based facilities, which was prior only achievable with space based observations. This development has opened up the time domain to be included in studies employing resolved scattered light imaging. This allows to trace the proper motions of substructures, such as spiral arms or dust-clumps, but also links the resolved observations to the inner, un-resolved disk regions via the variability of shadow features.

The proper motion of substructures gives insight into the mechanisms shaping the disk. For example, the rotation of spiral features has been the focus of attention. The angular velocity of the spirals can in this case be connected to the orbital distance of the perturbing body, that launches the spiral density wave in the gas. *Ren et al.* (2018) used a combination of HST/NICMOS, Keck/NIRC2 and VLT/SPHERE data to investigate the relative position of the spiral arms in MWC 758 over a time frame of more than 10 yr. They found that their measurements were best fit by a pattern speed of  $0.6_{-0.6}^{+3.3}$  deg yr $^{-1}$ . With five additional years of monitoring by VLT/SPHERE, they were eventually able to constrain this to  $0^{\circ}.22 \pm 0^{\circ}.03$  (*Ren et al.* 2020), corresponding to a planetary perturber at an orbit of  $\sim 172$  au. A similar pattern speed was found by *Boccaletti et al.* (2021), from their VLT/SPHERE data. This series of studies demonstrates the advancements in temporal studies enabled by

modern ground based instrumentation, with a dedicated astrometric calibration strategy (see e.g. *Maire et al.* 2016 for VLT/SPHERE). With growing time baseline we will in the future be able to trace the motion of most spiral features. The pattern speed, combined with the direction of motion (leading versus trailing spirals), will enable us to constrain the perturbing mechanism. Given the astrometric accuracy of currently available instrumentation, a motion such as in the spiral arms around MWC 758 can be detected within roughly two years.

As we discuss in section 5.2, azimuthal shadows are a common feature seen in scattered light observations. They enable us to draw conclusion on the inner disk geometry (typically inside of 10 au), which is inaccessible to current imaging observations, due to limited angular resolution. However, several studies have now found that the shadowing signatures on the outer disks are changing over time (*Debes et al.* 2017; *Stolker et al.* 2016b, 2017b; *Pinilla et al.* 2018). The timescales of some of these variations are as short as days, suggesting that dynamical processes in the innermost disk regions are responsible. Suggested processes include the precession of an inner disk due to a perturbing short-period planet or episodic accretion. These first studies motivate further monitoring in the future, in particular to detect periodicity and the shortest timescales of variation. Such monitoring campaigns may in the future be combined with near-IR interferometry, using the latest generation of instruments such as VLT/GRAVITY or VLT/MATISSE, to access the innermost disk regions.

## 7.2. Instrument upgrades and new facilities

Multiple avenues for further improving optical and IR imaging of circumstellar disks and embedded planets are on the horizon. The main dimensions for progress in observed systems are in total intensity calibration, wavelength coverage, contrast limits, and ultimately higher angular resolution (and smaller inner working angle) with the next-generation of Extremely Large Telescopes (ELTs). In addition to these gains, an important step forward will be to shift the optical brightness and thus stellar mass limitations of our current sample to the bulk of the low-mass star population which is already targeted by ALMA sub-mm surveys.

The vast majority of the high-contrast and high-fidelity disk imaging has been done in linear polarized intensity (PI, polarized intensity =  $Q^2 + U^2$ ) and often in only one or two passbands. The full potential of probing the dust size distribution in disks, a key diagnostic of planet formation processes, can only be unlocked with broad wavelength coverage and with PI images *calibrated with total intensity images*. While many "tricks" are effective in the searching for point sources (i.e., exoplanets) in messy total intensity imaging – through angular differential imaging (ADI), using chromatic properties of speckles, and/or use of reference image libraries (e.g., LOCI) – these methods fail for extended low surface brightness objects such as disks. The only path to improvement is through im-



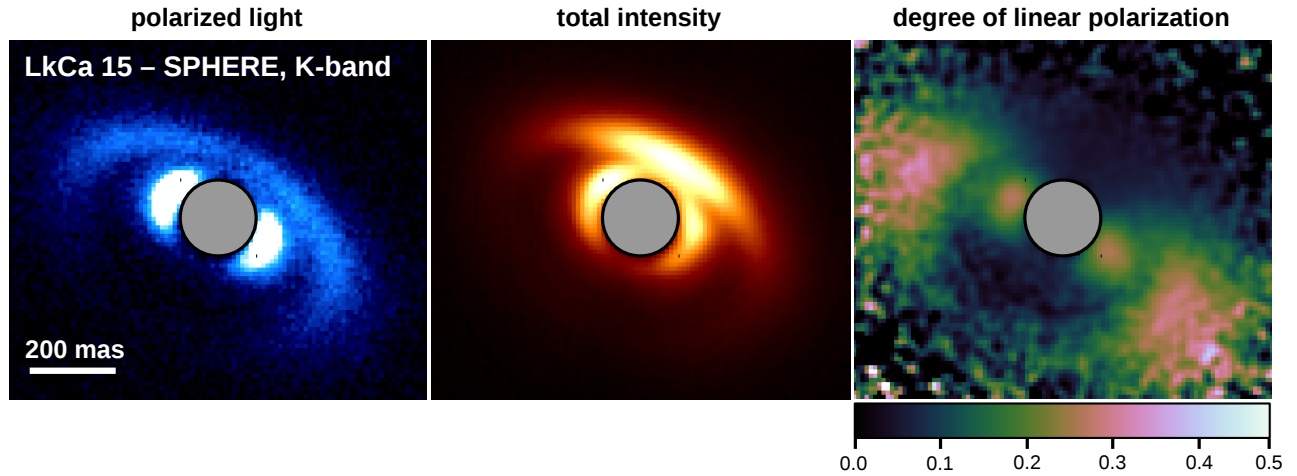


Fig. 17.— Recent VLT/SPHERE observation of the LkCa 15 system using a combination of the polarimetric imaging and the “star-hopping” mode for advanced reference differential imaging. The left panel shows polarized intensity and the middle panel shows total intensity. Both are displayed on a linear stretch of the color map which is a factor 10 larger for total intensity. The right panel shows the derived degree of linear polarization computed from the polarized intensity and total intensity image.

proved adaptive optics systems and/or *more stable and reproducible* performance stability to allow the stellar halo to be subtracted via either forward modeling or using contemporaneous observations of a reference source. While this method has been attempted for decades, there was recent progress demonstrated using VLT/SPHERE. Figure 17 presents polarized intensity and total intensity images of LkCa15, obtained simultaneously using the SPHERE star-hopping mode (Wahhaj et al. 2021) that allows interspersed observations of science target and a reference star with similar spectral properties. This rapid switching combined with the temporal stability of the adaptive optics system enables to obtain a near perfect library of reference star images, matching the scientific target. Combined with iterative post processing techniques that limit signal over-subtraction, this allows for significant improvements to the reference differential imaging technique. Obtaining both, the polarized and total intensity images, makes it possible to derive the degree of linear polarization, and further characterize the dust grains properties.

Other AO systems are also undergoing wavefront sensor upgrades, e.g., GPI2 (Chilcote et al. 2020), SPHERE+ (Boccaletti et al. 2020b), SCEXAO (Lozi et al. 2020), and MagAO-X (Males et al. 2020) in order to improve wavefront stability, peak strehl, and natural guide star sensitivity (especially, in the near-IR). In particular the last point, will unlock the bulk of the low-mass ( $<0.5 M_{\odot}$ ) stellar population in nearby star forming regions for observations, i.e. the most common members with the most typical compact disks. Embedded protoplanet studies will benefit from the same instrument upgrades, as well as the advancement of mid-to-high-resolution spectroscopic high-contrast imaging instruments such as MUSE and GRAVITY.

Even with PI and total-I imaging, the secrets of the dust populations require *multi-wavelength* observations. Optical

to near-IR wavelengths probe the characteristic dust sizes in the upper layers and can reveal important grain characteristics, including non-trivial properties arising from agglomerates rather than perfect Mie-scattering spheres. The scattering phase function can also be derived for disks with well-understood geometries, another probe of dust grain structure. Most protoplanetary disks lack the detailed phase-function work we have seen for some debris disks (e.g., HR4796 Arriaga et al. 2020). We might expect radial-, disk-height-, and age-dependence during the planet formation process and this represents a topic with immense potential. In addition to improved optical/near-IR coverage with existing AO instruments, mid-IR disk imaging from VLT/ERIS, VLT/CRIRES+, VLT/MATISSE will play an increasing role in disk studies.

Lastly, we look beyond the current instruments to the next-generation of telescopes. The James Webb Space Telescope will offer new high-contrast views of disks in the IR, although with a limited inner working angle. A stable point spread function should allow subtraction of the central star to reveal new details in nearby disks. Its sensitivity in near-IR atmospheric windows and in the MIR will enable studies of new and more sensitive accretion diagnostics. The Roman Space Telescope will have an experimental coronagraph operating in the optical that, while designed primarily for exoplanet science, will nonetheless offer an unprecedented view of circumstellar disks in the optical (Poberezhskiy et al. 2021) and will achieve  $H\alpha$  contrasts well below current ground-based limits (Mennesson et al. 2018). We hope for detection of the exoplanets that have been predicted for some disks based on analysis of the dust substructures. Beyond the relatively-small aperture space telescopes, we can look forward to the 30-m class telescopes under construction on Earth. While no polarization capabilities are under development for the first gener-

ation of ELT instruments, we expect the  $\sim 2 - 4\times$  boost in spatial resolution will allow important disk imaging with the following near-IR AO imagers: GMT/IRS, TMT/IRIS, and ELT/MICADO. Another exciting ELT instrument for disks is the mid-IR instrument ELT/METIS – bringing 50-milliarcsecond angular resolution to the  $10\mu\text{m}$  N band. The increased sensitivity and angular resolution of these instruments will allow direct detections of many young exoplanets (as well as proper motion studies) in nearby disks, finally revealing the links between planet formation and disk substructures such as spirals, rings, etc. Polarimetry has been mentioned for inclusion in some 2nd-generation, extreme AO instruments (e.g., TMT/PSI, ELT/PCS) but will likely not be available until  $>2035$ .

## 8. Summary

The years since PPVI have seen a revolution in the field of high spatial resolution, high contrast imaging of planet-forming disks and protoplanets. In addition to what ALMA has been able to achieve, direct imaging at optical and near-IR wavelengths have opened up a separate, complementary view. At the time of PPVI, we had the HST images of only a few planet-forming disks, and the Subaru telescope with the SEEDS program along with VLT/NACO had started to open up this space. While HST is still ruling supreme in terms of sensitivity at large working angles, the advancement of adaptive optics, advanced coronagraphy, and modern contrast-enhancing techniques on 8-10 m ground-based telescopes have made it possible to achieve detailed imaging at much smaller working angles. In the present chapter, we have described the outcome of this revolution. We summarize the key points of our review below.

1. The key contrast-enhancing technique has been Polarization Differential Imaging (PDI), allowing a very clean separation of disk photons from stellar (halo) photons without self-subtraction and the clearest detections of disk structures. Reference Differential Imaging allows access to total intensity, while Angular Differential Imaging drills down onto point sources, and Spectral Differential Imaging starts to give access to accretion-related line emission.
2. PDI observations allowed us to routinely image the disk portion from 15 au to 100 au that is hardly accessible by HST. Space observations do sometimes show a larger extent than that of the detectable polarized light, as also corroborated by the large size of gas disks seen with ALMA.
3. The overall flaring disk shape predicted in theoretical models for disks in hydrostatic equilibrium is commonly seen, and the shape of the disk surface can be measured if the disk has either ring-shaped features or a visible sharp outer edge.
4. The brightness of disks can vary significantly as a function of illumination geometry and grain proper-

ties, covering a range of at least a factor of 100 in luminosity-corrected brightness. The brightest disks have a dust-depleted cavity, leading to an enhanced illumination of the surface and inner rim of the remaining disk.

5. Measured scattering phase functions point to the existence of dust grains or more likely dust aggregates with sizes of several micrometers in the disk scattering surface. Some dust is still covered by water and possibly other ices.
6. Practically all bright and extended disks show a variety of structures: cavities, rings, spiral arms, both narrow and broad shadow features. Multiple rings are detected in many disks, with planets as origin speculated but unfortunately not yet confirmed. Spirals are more frequently found in early-type star disks, can be very prominent and sometimes be traced back to the interaction with a companion. Flocculent spirals which may result from gravitational instabilities or a multiple system in the disk are common as well. Narrow shadow lanes are traced back to highly inclined inner disks, while broad shadow features are probably related to disk warps of only a few degrees. Such misalignments and warps can be caused by inclined companions in the system, but also by late infall onto the disk, as evidenced in the observation of a number of disks. Some shadow features are variable in time, pointing to the role of surface height variations in the shadowing disk components.
7. Planetary or sub-stellar companions in disks can be found with imaging techniques, looking for the continuum emission of the object, line or continuum emission of a circumplanetary disk, kinematic disturbances in disk gas motions, or accretion-related emission lines. Just the detection of the PDS70 system with 2 directly detected planets has revolutionized the field. Many candidates still await confirmation and characterization, and an increase of the number of directly detected planets is arguably the most important goal for further research.

In the future, exceptional power will come from combining multiwavelength high angular resolution observations including scattered light, dust continuum and molecular line observations in similar detail on the same disks, in order to derive the strongest constraints on the properties and physical processes in disks, helping to decipher the environment in which planets for and planetary systems are shaped.

**Willy Kley****A tribute to a much-valued friend and colleague**

We have all lived through some difficult times during the last two years, but for his friends and colleagues one of the darkest days arrived on 21<sup>st</sup> December 2021 with the sad and unexpected news of Willy Kley's passing.

Willy will be missed by the science community for many reasons. For his contributions to our understanding of planet formation, and his pioneering work on disc-planet interactions. For his mentorship of students and early career researchers, many of whom are now leading researchers in the field, and for his exemplary commitment to university teaching. For his collegiality, generosity and fundamental decency as a human being.

Willy began his career in the late 1980s as a PhD student in Munich, where, with Gerhard Hensler, he introduced the use of hydrodynamical simulations to study accretion disc boundary layers in Cataclysmic Variables. Even at this early stage his papers exemplified the qualities that would become a hallmark of his later publications in planet formation: strongly motivated studies that address key questions in the field; development and deployment state-of-the-art numerical methods; results that lead to new insights, presented with a clear exposition.

Willy started to work on protoplanetary discs (PPDs) in the early 1990s when he was a postdoc in Santa Cruz working with Doug Lin. He and Doug visited London for a year in 1992, and collaborated with John Papaloizou on various problems in accretion disc theory, especially the role of convection in transporting angular momentum. Over the coming years Willy also published results on the hydrodynamics of boundary layers in PPDs and on FU Orionis outbursts.

The discovery of the first hot Jupiter, 51 Peg b, in 1995 changed everything, and the most important question of the moment became how do such systems actually form? Willy's expertise in PPDs and his finely-honed numerical skills, combined with his instinct for knowing which problems to work on, placed him in pole position to make an immediate impact, which he did with the publication in 1999 of one of his most influential papers *Mass flow and accre-*

*tion through gaps in accretion discs* (Kley 1999). For the next 20 years Willy would remain at the forefront of developments that have enhanced our understanding of planet formation and the role of disc-planet interactions.

Willy's scientific contributions, undertaken with many collaborators, are too numerous to detail, but highlights include: the first hydrodynamical study of a multi-planet system embedded in a PPD, followed up by later works on resonance capture to explain the GJ876 multi-planet system; pioneering studies of planet formation and evolution in close binary systems; ground-breaking studies of orbital evolution and gas accretion onto planets embedded in PPDs, employing state-of-the-art numerical methods, realistic equations of state and radiative processes; 3D radiation-hydrodynamic simulations of the Vertical Shear Instability and the settling/mixing of dust in the outer regions of PPDs. In addition, he contributed significantly to Protostar & Planets review articles, including those published as part of the PPV, PPVI and now PPVII conferences. In testament to his standing in the field, he was invited in 2012 to lead the publication of an Annual Reviews article on Disc-Planet Interaction and Orbital Evolution, which remains as a standard reference text on the topic.

My personal recollections of Willy go back to 1992 when he and Doug Lin visited Queen Mary University of London (QMUL) where I was as a PhD student. I had the impossible task of running star formation simulations on the ageing computers we had in the department at QMUL. Thankfully, Willy and Doug had brought with them the latest IBM workstation from Santa Cruz, along with a substantial allocation of time at the San Diego supercomputing centre. As soon as Willy realised my situation, and without prompting or hesitation, he gave me access to both of these resources, literally enabling me to complete my PhD in the process. This act of generosity was the start of a life-long friendship. Willy and I started collaborating scientifically in the late 1990s, by which time we were both working on the problem of disc-planet interactions. Once again I was in receipt of Willy's generosity when he offered to share his simulation code, which was far superior to the method I was using at the time. Working with Willy was always a pleasure, and I recall with great fondness the many wide-ranging discussions we had in restaurants and bars at conferences, or over weissbier and schweinshaxe during my numerous visits to Tübingen. He had many qualities as a collaborator and a scientist, but the one that stands out most of all was his love of science and dedication to understanding the world we live in.

Outside of work Willy was a loving and committed husband and father, and is survived by his wife, Martina, and his daughters Lily, Xenia and Sian. He will be missed but not forgotten.

Richard P. Nelson  
March 10, 2022

**Acknowledgments** We are very grateful to Evan Rich for his help with the GPI datasets and the uniformization of the FITS format for direct imaging data, and to Ryo Tazaki for his help in shaping Section 4.3 and for providing Figure 6. We thank Jaehan Bae for fruitful discussions about substructures while writing the review. We acknowledge undergraduate researchers Alexander DelFranco and Dane Mansfield of Amherst College for their contributions to the design of Figure 1, and Vanessa Bailey for her public code used to generate Figure 14. We thank the three reviewers whose extensive reviews, detailed comments and constructive suggestions helped improve the manuscript. We acknowledge the essential contribution of scientists, engineers, astronomers, telescope operators, working at the VLT, Subaru and Gemini facilities, and for the HST, who allow the community to obtain the results presented in this review. This project has received funding from the European Research Council (ERC) under the European Union’s Horizon 2020 research and innovation programme (PRO-TOPLANETS, grant agreement No. 101002188). JDM acknowledges support from NSF/AST-1830728, and KBF from NSF/AST-2009816. C.G. and C.D acknowledge funding from the Netherlands Organisation for Scientific Research (NWO), project number 614.001.552.

## REFERENCES

- Alcalá J. M. et al., 2017 *A&A*, 600, A20.  
 ALMA Partnership et al., 2015 *ApJL*, 808, 1, L3.  
 Amara A. and Quanz S. P., 2012 *MNRAS*, 427, 948.  
 Andersson B. G. et al., 2015 *ARA&A*, 53, 501.  
 Andrews S. M., 2020 *ARA&A*, 58, 483.  
 Andrews S. M. et al., 2016 *ApJL*, 820, 2, L40.  
 Andrews S. M. et al., 2018 *ApJ*, 869, 2, L41.  
 Andrews S. M. et al., 2021 *ApJ*, 916, 1, 51.  
 Ansdell M. et al., 2016 *ApJ*, 828, 46.  
 Aoyama Y. et al., 2018 *ApJ*, 866, 2, 84.  
 Aoyama Y. et al., 2020 *arXiv e-prints*, arXiv:2011.06608.  
 Apai D. et al., 2004 *A&A*, 415, 671.  
 Arriaga P. et al., 2020 *AJ*, 160, 2, 79.  
 Asensio-Torres R. et al., 2021 *A&A*, 652, A101.  
 Avenhaus H. et al., 2014a *ApJ*, 790, 56.  
 Avenhaus H. et al., 2014b *ApJ*, 781, 87.  
 Avenhaus H. et al., 2017 *AJ*, 154, 1, 33.  
 Avenhaus H. et al., 2018 *ApJ*, 863, 1, 44.  
 Babcock H. W., 1953 *PASP*, 65, 386, 229.  
 Bae J. et al., 2017 *ApJ*, 850, 2, 201.  
 Bae J. et al., 2018 *ApJL*, 864, 2, L26.  
 Bae J. et al., 2019 *ApJL*, 884, 2, L41.  
 Bagnulo S. et al., 2009 *PASP*, 121, 883, 993.  
 Ballabio G. et al., 2021 *MNRAS*, 504, 1, 888.  
 Barraza-Alfaro M. et al., 2021 *A&A*, 653, A113.  
 Baruteau C. et al., 2019 *MNRAS*, 486, 1, 304.  
 Batygin K. and Morbidelli A., 2013 *AJ*, 145, 1.  
 Batygin K. and Morbidelli A., 2020 *ApJ*, 894, 2, 143.  
 Beichman C. A. et al., 2010 *PASP*, 122, 888, 162.  
 Benisty M. et al., 2015 *A&A*, 578, L6.  
 Benisty M. et al., 2017 *A&A*, 597, A42.  
 Benisty M. et al., 2018 *A&A*, 619, A171.  
 Benisty M. et al., 2021 *ApJL*, 916, 1, L2.  
 Bertrang G. H.-M. et al., 2018 *MNRAS*, 474, 5105.  
 Béthune W. et al., 2016 *A&A*, 589, A87.  
 Béthune W. et al., 2017 *A&A*, 600, A75.  
 Béthune W. et al., 2021 *A&A*, 650, A49.  
 Beuzit J. L. et al., 2019 *A&A*, 631, A155.  
 Biller B. A. et al., 2014 *ApJL*, 792, L22.  
 Birnstiel T. et al., 2010 *A&A*, 513, A79.  
 Bitsch B. et al., 2013 *A&A*, 555, A124.  
 Blanco D. et al., 2021 *ApJ*, 920, 2, 70.  
 Boccaletti A. et al., 2020a *A&A*, 637, L5.  
 Boccaletti A. et al., 2020b *arXiv e-prints*, arXiv:2003.05714.  
 Boccaletti A. et al., 2021 *A&A*, 652, L8.  
 Bodman E. H. L. et al., 2017 *MNRAS*, 470, 1, 202.  
 Bohn A. J. et al., 2019 *A&A*, 624, A87.  
 Bohn A. J. et al., 2021 *arXiv e-prints*, arXiv:2112.00123.  
 Bouvier J. et al., 1999 *A&A*, 349, 619.  
 Brittain S. D. et al., 2013 *ApJ*, 767, 159.  
 Brown-Sevilla S. B. et al., 2021 *A&A*, 654, A35.  
 Bryden G. et al., 1999 *ApJ*, 514, 1, 344.  
 Burrows C. J. et al., 1996 *ApJ*, 473, 437.  
 Calcino J. et al., 2020 *MNRAS*, 498, 1, 639.  
 Canovas H. et al., 2011 *A&A*, 531, A102.  
 Canovas H. et al., 2013 *A&A*, 556, A123.  
 Canovas H. et al., 2015 *A&A*, 582, L7.  
 Canovas H. et al., 2018 *A&A*, 610, A13.  
 Cantalloube F. et al., 2019 *The Messenger*, 176, 25.  
 Casassus S. and Pérez S., 2019 *ApJL*, 883, 2, L41.  
 Casassus S. et al., 2013 *Nature*, 493, 7431, 191.  
 Casassus S. et al., 2018 *MNRAS*, 477, 4, 5104.  
 Cazzoletti P. et al., 2018 *A&A*, 619, A161.  
 Chauvin G. et al., 2017 *SF2A-2017: Proceedings of the Annual meeting of the French Society of Astronomy and Astrophysics* (C. Reylé, P. Di Matteo, F. Herpin, E. Lagadec, A. Lançon, Z. Meliani, and F. Royer), pp. 331–335.  
 Chiang E. I. and Goldreich P., 1997 *ApJ*, 490, 1, 368.  
 Chilcote J. et al., 2020 *Society of Photo-Optical Instrumentation Engineers (SPIE) Conference Series*, vol. 11447 of *Society of Photo-Optical Instrumentation Engineers (SPIE) Conference Series*, p. 114471S.  
 Choquet É. et al., 2014 *Space Telescopes and Instrumentation 2014: Optical, Infrared, and Millimeter Wave*, vol. 9143 of *Society of Photo-Optical Instrumentation Engineers (SPIE) Conference Series* (J. Oschmann Jacobus M., M. Clampin, G. G. Fazio, and H. A. MacEwen), p. 914357.  
 Choquet É. et al., 2016 *ApJL*, 817, 1, L2.  
 Christiaens V. et al., 2019 *ApJL*, 877, 2, L33.  
 Ciesla F. J. and Cuzzi J. N., 2006 *Icarus*, 181, 1, 178.  
 Clampin M. et al., 2003 *AJ*, 126, 385.  
 Claudi R. U. et al., 2008 *Ground-based and Airborne Instrumentation for Astronomy II*, vol. 7014 of *Society of Photo-Optical Instrumentation Engineers (SPIE) Conference Series* (I. S. McLean and M. M. Casali), p. 70143E.  
 Cody A. M. et al., 2014 *AJ*, 147, 4, 82.  
 Cossins P. et al., 2009 *MNRAS*, 393, 4, 1157.  
 Crida A. et al., 2006 *Icarus*, 181, 2, 587.  
 Cugno G. et al., 2019 *A&A*, 622, A156.  
 Cugno G. et al., 2021 *A&A*, 653, A12.  
 Currie T. et al., 2015 *ApJL*, 814, L27.  
 Currie T. et al., 2019 *ApJL*, 877, 1, L3.  
 Davis Leverett J. and Greenstein J. L., 1951 *ApJ*, 114, 206.  
 de Boer J. et al., 2016 *A&A*, 595, A114.

- de Boer J. et al., 2020 *A&A*, 633, A63.
- de Boer J. et al., 2021 *A&A*, 649, A25.
- de Juan Ovelar M. et al., 2013 *A&A*, 560, A111.
- de Val-Borro M. et al., 2006 *MNRAS*, 370, 2, 529.
- Debes J. H. et al., 2017 *ApJ*, 835, 2, 205.
- Dolginov A. Z. and Mitrofanov I. G., 1976 *Ap&SS*, 43, 2, 291.
- Dominik C. et al., 2007 *Protostars and Planets V* (B. Reipurth, D. Jewitt, and K. Keil), p. 783.
- Dong R. and Fung J., 2017 *ApJ*, 835, 2, 146.
- Dong R. et al., 2012a *ApJ*, 750, 2, 161.
- Dong R. et al., 2012b *ApJ*, 760, 2, 111.
- Dong R. et al., 2015a *ApJ*, 809, 1, 93.
- Dong R. et al., 2015b *ApJL*, 809, 1, L5.
- Dong R. et al., 2016a *ApJ*, 826, 1, 75.
- Dong R. et al., 2016b *ApJ*, 826, 1, 75.
- Dong R. et al., 2017 *ApJ*, 843, 2, 127.
- Dong R. et al., 2018 *ApJ*, 860, 2, 124.
- Dong R. et al., 2019 *ApJ*, 870, 2, 72.
- Draine B. T. and Weingartner J. C., 1996 *ApJ*, 470, 551.
- Draine B. T. and Weingartner J. C., 1997 *ApJ*, 480, 2, 633.
- Duchêne G. et al., 2004 *ApJ*, 606, 2, 969.
- Dullemond C. P. and Dominik C., 2005 *A&A*, 434, 3, 971.
- Dullemond C. P. et al., 2001 *ApJ*, 560, 957.
- Dullemond C. P. et al., 2002 *A&A*, 389, 464.
- Dullemond C. P. et al., 2018 *ApJL*, 869, 2, L46.
- Dullemond C. P. et al., 2019 *A&A*, 628, A20.
- Dutrey A. et al., 1994 *A&A*, 286, 149.
- Dutrey A. et al., 2014 *Protostars and Planets VI* (H. Beuther, R. S. Klessen, C. P. Dullemond, and T. Henning), p. 317.
- Dzib S. A. et al., 2018 *ApJ*, 867, 2, 151.
- Eisner J. A., 2015 *ApJL*, 803, 1, L4.
- Espaillat C. et al., 2011 *ApJ*, 728, 49.
- Espaillat C. et al., 2014 *Protostars and Planets VI* (H. Beuther, R. S. Klessen, C. P. Dullemond, and T. Henning), p. 497.
- Facchini S. et al., 2013 *MNRAS*, 433, 3, 2142.
- Facchini S. et al., 2018 *MNRAS*, 473, 4, 4459.
- Facchini S. et al., 2020 *A&A*, 639, A121.
- Follette K. B. et al., 2013 *ApJ*, 767, 10.
- Follette K. B. et al., 2015 *ApJ*, 798, 132.
- Follette K. B. et al., 2017 *AJ*, 153, 6, 264.
- Fukagawa M. et al., 2004 *ApJL*, 605, 1, L53.
- Fukagawa M. et al., 2006 *ApJL*, 636, 2, L153.
- Fukagawa M. et al., 2010 *PASJ*, 62, 347.
- Fukue T. et al., 2010 *Origins of Life and Evolution of the Biosphere*, 40, 335.
- Fung J. et al., 2014 *ApJ*, 782, 2, 88.
- Fusco T. et al., 2006 *Society of Photo-Optical Instrumentation Engineers (SPIE) Conference Series*, vol. 6272 of *Society of Photo-Optical Instrumentation Engineers (SPIE) Conference Series*, p. 0.
- Gaia Collaboration et al., 2020 *arXiv e-prints*, arXiv:2012.01533.
- Garufi A. et al., 2013 *A&A*, 560, A105.
- Garufi A. et al., 2014 *A&A*, 568, A40.
- Garufi A. et al., 2016 *A&A*, 588, A8.
- Garufi A. et al., 2017 *A&A*, 603, A21.
- Garufi A. et al., 2018 *A&A*, 620, A94.
- Garufi A. et al., 2020 *A&A*, 633, A82.
- Garufi A. et al., 2022 *A&A*, 658, A137.
- Ginski C. et al., 2016 *A&A*, 595, A112.
- Ginski C. et al., 2018 *A&A*, 616, A79.
- Ginski C. et al., 2020 *A&A*, 642, A119.
- Ginski C. et al., 2021a *arXiv e-prints*, arXiv:2111.11077.
- Ginski C. et al., 2021b *ApJL*, 908, 2, L25.
- Gledhill T. M. and McCall A., 2000 *MNRAS*, 314, 1, 123.
- Gonzalez J.-F. et al., 2020 *MNRAS*, 499, 3, 3837.
- Grady C. A. et al., 1999 *ApJL*, 523, L151.
- Grady C. A. et al., 2000 *ApJ*, 544, 895.
- Grady C. A. et al., 2001 *AJ*, 122, 3396.
- Grady C. A. et al., 2005 *ApJ*, 620, 470.
- Grady C. A. et al., 2009 *ApJ*, 699, 1822.
- Grady C. A. et al., 2013 *ApJ*, 762, 48.
- Graham J. R. et al., 2007 *ApJ*, 654, 1, 595.
- Gratton R. et al., 2019 *A&A*, 623, A140.
- Gravity Collaboration et al., 2021 *A&A*, 654, A97.
- Groff T. D. et al., 2015 *Techniques and Instrumentation for Detection of Exoplanets VII*, vol. 9605 of *Society of Photo-Optical Instrumentation Engineers (SPIE) Conference Series* (S. Shakhlan), p. 96051C.
- Guidi G. et al., 2018 *MNRAS*, 479, 2, 1505.
- Guyon O., 2018 *ARA&A*, 56, 315.
- Guzmán V. V. et al., 2018 *ApJ*, 864, 2, 170.
- Haffert S. Y. et al., 2019 *Nature Astronomy*, 3, 749.
- Hartmann L. et al., 2016 *ARA&A*, 54, 135.
- Hashimoto J. et al., 2011 *ApJL*, 729, L17.
- Hashimoto J. et al., 2012 *ApJL*, 758, L19.
- Hashimoto J. et al., 2015 *ApJ*, 799, 1, 43.
- Hashimoto J. et al., 2020 *AJ*, 159, 5, 222.
- Honda M. et al., 2009 *ApJL*, 690, 2, L110.
- Honda M. et al., 2015 *ApJ*, 804, 143.
- Honda M. et al., 2016 *ApJ*, 821, 1, 2.
- Hughes A. M. et al., 2018 *ARA&A*, 56, 541.
- Hunziker S. et al., 2021 *A&A*, 648, A110.
- Isella A. et al., 2018 *ApJL*, 869, 2, L49.
- Isella A. et al., 2019 *ApJL*, 879, 2, L25.
- Itoh Y. et al., 2002 *PASJ*, 54, 963.
- Itoh Y. et al., 2014 *Research in Astronomy and Astrophysics*, 14, 1438-1446.
- Izquierdo A. F. et al., 2021a *arXiv e-prints*, arXiv:2111.06367.
- Izquierdo A. F. et al., 2021b *A&A*, 650, A179.
- Jorquera S. et al., 2021 *AJ*, 161, 3, 146.
- Jovanovic N. et al., 2015 *PASP*, 127, 955, 890.
- Juhász A. et al., 2015 *MNRAS*, 451, 1147.
- Kanagawa K. D. et al., 2015 *ApJL*, 806, 1, L15.
- Kenyon S. J. and Hartmann L., 1987 *ApJ*, 323, 714.
- Keppler M. et al., 2018 *A&A*, 617, A44.
- Keppler M. et al., 2019 *A&A*, 625, A118.
- Keppler M. et al., 2020a *A&A*, 639, A62.
- Keppler M. et al., 2020b *A&A*, 639, A62.
- Klahr H. H. and Bodenheimer P., 2003 *ApJ*, 582, 2, 869.
- Kley W., 1999 *MNRAS*, 303, 4, 696.
- Kley W. et al., 2001 *ApJ*, 547, 1, 457.
- Kostov V. B. et al., 2016 *ApJ*, 827, 1, 86.
- Kozasa T. et al., 1993 *A&A*, 276, 278.
- Kraus A. L. and Ireland M. J., 2012a *ApJ*, 745, 5.
- Kraus A. L. and Ireland M. J., 2012b *ApJ*, 745, 1, 5.
- Kraus S. et al., 2020 *Science*, 369, 6508, 1233.
- Krist J. E. et al., 2000 *ApJ*, 538, 2, 793.
- Krist J. E. et al., 2002 *ApJ*, 570, 2, 785.
- Krivova N. A. et al., 2000 *ApJ*, 539, 1, 424.
- Kuhn J. R. et al., 2001 *ApJL*, 553, 2, L189.
- Kusakabe N. et al., 2012 *ApJ*, 753, 153.
- Kwon J. et al., 2013 *ApJL*, 765, 1, L6.
- Kwon J. et al., 2014 *ApJL*, 795, 1, L16.
- Kwon J. et al., 2016a *AJ*, 152, 3, 67.



- Kwon J. et al., 2016b *ApJ*, 824, 2, 95.
- Kwon J. et al., 2018 *AJ*, 156, 1, 1.
- Labdon A. et al., 2019 *A&A*, 627, A36.
- Lafrenière D. et al., 2007 *ApJ*, 660, 770.
- Lagage P.-O. et al., 2006 *Science*, 314, 621.
- Langlois M. et al., 2018 *A&A*, 614, A88.
- Larkin J. E. et al., 2014 *Ground-based and Airborne Instrumentation for Astronomy V*, vol. 9147 of *Society of Photo-Optical Instrumentation Engineers (SPIE) Conference Series* (S. K. Ramsay, I. S. McLean, and H. Takami), p. 91471K.
- Launhardt R. et al., 2020 *A&A*, 635, A162.
- Laws A. S. E. et al., 2020 *ApJ*, 888, 1, 7.
- Lesur G. and Papaloizou J. C. B., 2010 *A&A*, 513, A60.
- Li H. et al., 2005 *ApJ*, 624, 2, 1003.
- Ligi R. et al., 2018 *MNRAS*, 473, 2, 1774.
- Lissauer J. J. et al., 2011 *ApJS*, 197, 1, 8.
- Lodato G. et al., 2019 *MNRAS*, 486, 1, 453.
- Long F. et al., 2018 *ApJ*, 863, 1, 61.
- Lorén-Aguilar P. and Bate M. R., 2015 *MNRAS*, 453, 1, L78.
- Lovelace R. V. E. et al., 1999 *ApJ*, 513, 2, 805.
- Lozi J. et al., 2020 *Society of Photo-Optical Instrumentation Engineers (SPIE) Conference Series*, vol. 11448 of *Society of Photo-Optical Instrumentation Engineers (SPIE) Conference Series*, p. 114480N.
- Lucas P. W. et al., 2005 *Origins of Life and Evolution of the Biosphere*, 35, 1, 29.
- Luhman K. L., 2018 *AJ*, 156, 6, 271.
- Maaskant K. M. et al., 2013 *A&A*, 555, A64.
- Macintosh B. et al., 2006 *Society of Photo-Optical Instrumentation Engineers (SPIE) Conference Series*, vol. 6272 of *Society of Photo-Optical Instrumentation Engineers (SPIE) Conference Series* (B. L. Ellerbroek and D. Bonaccini Calia), p. 62720L.
- Macintosh B. et al., 2014 *Proceedings of the National Academy of Science*, 111, 12661.
- Maire A. L. et al., 2016 *A&A*, 587, A56.
- Males J. R. et al., 2020 *Society of Photo-Optical Instrumentation Engineers (SPIE) Conference Series*, vol. 11448 of *Society of Photo-Optical Instrumentation Engineers (SPIE) Conference Series*, p. 114484L.
- Manara C. F. et al., 2014 *A&A*, 568, A18.
- Manger N. et al., 2020 *MNRAS*, 499, 2, 1841.
- Marino S. et al., 2015 *ApJL*, 798, L44.
- Marois C. et al., 2006 *ApJ*, 641, 556.
- Marois C. et al., 2008 *Science*, 322, 5906, 1348.
- Martin R. G. et al., 2016 *MNRAS*, 458, 4, 4345.
- Matsakos T. and Königl A., 2017 *AJ*, 153, 2, 60.
- Maucó K. et al., 2020 *MNRAS*, 492, 2, 1531.
- Mayama S. et al., 2012 *ApJL*, 760, L26.
- Mayama S. et al., 2020 *AJ*, 159, 1, 12.
- McCabe C. et al., 2002 *ApJ*, 575, 2, 974.
- Meeus G. et al., 2001 *A&A*, 365, 476.
- Meheut H. et al., 2010 *A&A*, 516, A31.
- Ménard F. et al., 2020 *A&A*, 639, L1.
- Mendigutía I. et al., 2018 *A&A*, 618, L9.
- Mennesson B. et al., 2018 *Space Telescopes and Instrumentation 2018: Optical, Infrared, and Millimeter Wave*, vol. 10698 of *Society of Photo-Optical Instrumentation Engineers (SPIE) Conference Series* (M. Lystrup, H. A. MacEwen, G. G. Fazio, N. Batalha, N. Siegler, and E. C. Tong), p. 106982I.
- Mesa D. et al., 2019a *A&A*, 624, A4.
- Mesa D. et al., 2019b *A&A*, 632, A25.
- Mesa D. et al., 2022 *A&A*, 658, A63.
- Milli J. et al., 2012 *A&A*, 545, A111.
- Milli J. et al., 2017 *A&A*, 599, A108.
- Miranda R. and Rafikov R. R., 2019 *ApJL*, 878, 1, L9.
- Momose M. et al., 2015 *PASJ*, 67, 5, 83.
- Monnier J. D. et al., 2017 *ApJ*, 838, 20.
- Monnier J. D. et al., 2019 *ApJ*, 872, 2, 122.
- Mordasini C. et al., 2017 *A&A*, 608, A72.
- Mouillet D. et al., 2001 *A&A*, 372, L61.
- Muñoz O. et al., 2017 *ApJ*, 846, 1, 85.
- Mulders G. D. et al., 2013 *A&A*, 549, A112.
- Müller A. et al., 2018a *A&A*, 617, L2.
- Müller A. et al., 2018b *A&A*, 617, L2.
- Murakawa K., 2010 *A&A*, 518, A63.
- Murakawa K. et al., 2008 *A&A*, 492, 3, 731.
- Muro-Arena G. A. et al., 2018 *A&A*, 614, A24.
- Muro-Arena G. A. et al., 2020 *A&A*, 635, A121.
- Muto T. et al., 2012 *ApJL*, 748, L22.
- Nakajima T. and Golimowski D. A., 1995 *AJ*, 109, 1181.
- Nealon R. et al., 2018 *MNRAS*, 481, 1, 20.
- Nealon R. et al., 2019 *MNRAS*, 484, 4, 4951.
- Nealon R. et al., 2020 *MNRAS*, 499, 3, 3857.
- Nelson R. P. et al., 2013 *MNRAS*, 435, 3, 2610.
- O'Dell C. R. and Wen Z., 1994 *ApJ*, 436, 194.
- O'Dell C. R. et al., 1993 *ApJ*, 410, 696.
- Ogihara M. et al., 2018 *A&A*, 615, A63.
- Ogilvie G. I. and Lubow S. H., 2002 *MNRAS*, 330, 4, 950.
- Ohta Y. et al., 2016 *PASJ*, 68, 53.
- Okuzumi S. et al., 2012 *ApJ*, 752, 2, 106.
- Ossenkopf V. and Henning T., 1994 *A&A*, 291, 943.
- Owen J. E. and Lai D., 2017 *MNRAS*, 469, 3, 2834.
- Paardekooper S. J. and Mellema G., 2006 *A&A*, 453, 3, 1129.
- Padgett D. L. et al., 1999 *AJ*, 117, 3, 1490.
- Pantín E. et al., 2000 *A&A*, 361, L9.
- Perez S. et al., 2015 *ApJL*, 811, 1, L5.
- Pérez S. et al., 2020 *ApJL*, 889, 1, L24.
- Perrin M. D. et al., 2006 *ApJ*, 645, 2, 1272.
- Perrin M. D. et al., 2009 *ApJL*, 707, L132.
- Perrin M. D. et al., 2015 *ApJ*, 799, 2, 182.
- Perrot C. et al., 2016 *A&A*, 590, L7.
- Pinilla P. et al., 2012 *A&A*, 545, A81.
- Pinilla P. et al., 2015 *A&A*, 580, A105.
- Pinilla P. et al., 2017 *ApJ*, 845, 1, 68.
- Pinilla P. et al., 2018 *ApJ*, 868, 2, 85.
- Pinte C. et al., 2008 *A&A*, 489, 633.
- Pinte C. et al., 2018 *ApJL*, 860, 1, L13.
- Pinte C. et al., 2019 *Nature Astronomy*, 3, 1109.
- Pinte C. et al., 2020 *ApJL*, 890, 1, L9.
- Poberezhskiy I. et al., 2021 *Space Telescopes and Instrumentation 2020: Optical, Infrared, and Millimeter Wave*, vol. 11443 of *Society of Photo-Optical Instrumentation Engineers (SPIE) Conference Series*, p. 114431V.
- Pohl A. et al., 2017 *ApJ*, 850, 52.
- Pollack J. B. et al., 1996 *Icarus*, 124, 1, 62.
- Poteet C. A. et al., 2018 *ApJ*, 860, 2, 115.
- Price D. J. et al., 2018 *MNRAS*, 477, 1, 1270.
- Qi C. et al., 2011 *ApJ*, 740, 84.
- Quanz S. P. et al., 2011 *ApJ*, 738, 23.
- Quanz S. P. et al., 2012 *A&A*, 538, A92.
- Quanz S. P. et al., 2013a *ApJL*, 766, L1.
- Quanz S. P. et al., 2013b *ApJL*, 766, L2.
- Quanz S. P. et al., 2015a *ApJ*, 807, 64.

- Quanz S. P. et al., 2015b *ApJ*, 807, 1, 64.
- Ragusa E. et al., 2017 *MNRAS*, 464, 2, 1449.
- Rameau J. et al., 2017a *AJ*, 153, 6, 244.
- Rameau J. et al., 2017b *AJ*, 153, 6, 244.
- Rapson V. A. et al., 2015 *ApJL*, 803, L10.
- Regály Z. and Vorobyov E., 2017 *MNRAS*, 471, 2, 2204.
- Reggiani M. et al., 2014 *ApJL*, 792, L23.
- Reggiani M. et al., 2018 *A&A*, 611, A74.
- Ren B. et al., 2018 *ApJL*, 857, 1, L9.
- Ren B. et al., 2020 *ApJL*, 898, 2, L38.
- Riaud P. et al., 2006 *A&A*, 458, 1, 317.
- Rich E. A. et al., 2019 *ApJ*, 875, 1, 38.
- Rich E. A. et al., 2020 *ApJ*, 902, 1, 4.
- Rich E. A. et al., 2021 *ApJ*, 913, 2, 138.
- Richard S. et al., 2016 *MNRAS*, 456, 4, 3571.
- Rigliaco E. et al., 2012 *A&A*, 548, A56.
- Rigliaco E. et al., 2020 *A&A*, 641, A33.
- Riols A. and Lesur G., 2019 *A&A*, 625, A108.
- Riols A. et al., 2020a *A&A*, 639, A95.
- Riols A. et al., 2020b *A&A*, 639, A95.
- Roddiar C. et al., 1996 *ApJ*, 463, 326.
- Rosenfeld K. A. et al., 2014 *ApJ*, 782, 2, 62.
- Rosotti G. P. et al., 2020 *MNRAS*, 491, 1, 1335.
- Ruge J. P. et al., 2016 *A&A*, 590, A17.
- Sallum S. et al., 2015 *Nature*, 527, 7578, 342.
- Sallum S. et al., 2016 *Optical and Infrared Interferometry and Imaging V*, vol. 9907 of *Society of Photo-Optical Instrumentation Engineers (SPIE) Conference Series* (F. Malbet, M. J. Creech-Eakman, and P. G. Tuthill), p. 99070D.
- Schmid H. M. et al., 2018 *A&A*, 619, A9.
- Schneider G. and Silverstone M. D., 2003 *High-Contrast Imaging for Exo-Planet Detection.*, vol. 4860 of *Society of Photo-Optical Instrumentation Engineers (SPIE) Conference Series* (A. B. Schultz), pp. 1–9.
- Schneider G. et al., 2014 *AJ*, 148, 4, 59.
- Setterholm B. R. et al., 2018 *ApJ*, 869, 2, 164.
- Sicilia-Aguilar A. et al., 2020 *A&A*, 633, A37.
- Silber J. et al., 2000 *ApJL*, 536, 2, L89.
- Sissa E. et al., 2018 *A&A*, 619, A160.
- Snik F. and Keller C. U., 2013 *Planets, Stars and Stellar Systems. Volume 2: Astronomical Techniques, Software and Data* (T. D. Oswalt and H. E. Bond), p. 175, Springer.
- Soummer R. et al., 2012 *ApJL*, 755, L28.
- Stamatellos D. and Herczeg G. J., 2015 *MNRAS*, 449, 4, 3432.
- Stapelfeldt K. R. et al., 1998 *ApJL*, 502, 1, L65.
- Stapelfeldt K. R. et al., 2003 *ApJ*, 589, 1, 410.
- Stapelfeldt K. R. et al., 2014 *Exploring the Formation and Evolution of Planetary Systems*, vol. 299 (M. Booth, B. C. Matthews, and J. R. Graham), pp. 99–103.
- Stokes G. G., 1851 *Transactions of the Cambridge Philosophical Society*, 9, 399.
- Stolker T. et al., 2016a *A&A*, 596, A70.
- Stolker T. et al., 2016b *A&A*, 595, A113.
- Stolker T. et al., 2017a *A&A*, 607, A42.
- Stolker T. et al., 2017b *ApJ*, 849, 2, 143.
- Stolker T. et al., 2020 *A&A*, 644, A13.
- Stone J. M. et al., 2018 *AJ*, 156, 6, 286.
- Strom K. M. et al., 1989 *AJ*, 97, 1451.
- Suzuki T. K. and Inutsuka S.-i., 2009 *ApJL*, 691, 1, L49.
- Suzuki T. K. et al., 2016 *A&A*, 596, A74.
- Szulágyi J. and Garufi A., 2021 *MNRAS*, 506, 1, 73.
- Szulágyi J. et al., 2019a *MNRAS*, 487, 1, 1248.
- Szulágyi J. et al., 2019b *MNRAS*, 487, 1, 1248.
- Takami M. et al., 2013 *ApJ*, 772, 145.
- Takami M. et al., 2014 *ApJ*, 795, 71.
- Tamura M., 2016 *Proceedings of the Japan Academy, Series B*, 92, 45.
- Tamura M. et al., 2006 *Society of Photo-Optical Instrumentation Engineers (SPIE) Conference Series*, vol. 6269 of *Society of Photo-Optical Instrumentation Engineers (SPIE) Conference Series* (I. S. McLean and M. Iye), p. 62690V.
- Tang Y.-W. et al., 2017 *ApJ*, 840, 32.
- Tanigawa T. et al., 2012 *ApJ*, 747, 1, 47.
- Tanii R. et al., 2012 *PASJ*, 64, 124.
- Tazaki R. et al., 2017 *ApJ*, 839, 1, 56.
- Tazaki R. et al., 2019 *MNRAS*, 485, 4, 4951.
- Tazaki R. et al., 2021 *ApJ*, 910, 1, 26.
- Teague R. et al., 2019 *Nature*, 574, 7778, 378.
- Thalmann C. et al., 2010 *ApJL*, 718, 2, L87.
- Thalmann C. et al., 2015 *ApJL*, 808, L41.
- Thalmann C. et al., 2016 *ApJL*, 828, L17.
- Thun D. et al., 2017 *A&A*, 604, A102.
- Toci C. et al., 2020 *MNRAS*, 499, 2, 2015.
- Tschudi C. and Schmid H. M., 2021 *A&A*, 655, A37.
- Uyama T. et al., 2017 *AJ*, 153, 3, 106.
- Uyama T. et al., 2018 *AJ*, 156, 2, 63.
- Uyama T. et al., 2020 *AJ*, 159, 3, 118.
- van Boekel R. et al., 2017 *ApJ*, 837, 132.
- van der Marel N. et al., 2016 *ApJ*, 832, 2, 178.
- van der Marel N. et al., 2021 *AJ*, 161, 1, 33.
- van Holstein R. G. et al., 2020 *A&A*, 633, A64.
- van Holstein R. G. et al., 2021 *A&A*, 647, A21.
- Varga J. et al., 2021 *A&A*, 647, A56.
- Vigan A. et al., 2015 *MNRAS*, 454, 1, 129.
- Villeneuve M. et al., 2019 *A&A*, 624, A7.
- Villeneuve M. et al., 2020 *A&A*, 642, A164.
- Wada K. et al., 2011 *ApJ*, 737, 1, 36.
- Wafflard-Fernandez G. and Baruteau C., 2020 *MNRAS*, 493, 4, 5892.
- Wagner K. et al., 2015 *ApJL*, 813, L2.
- Wagner K. et al., 2018 *ApJL*, 863, 1, L8.
- Wagner K. et al., 2019 *ApJ*, 882, 1, 20.
- Wahhaj Z. et al., 2021 *A&A*, 648, A26.
- Walker S. et al., 2021 *MNRAS*, 504, 2, 3074.
- Wang J. J. et al., 2020 *AJ*, 159, 6, 263.
- Wang J. J. et al., 2021 *AJ*, 161, 3, 148.
- Watson A. M. et al., 2007 *Protostars and Planets V* (B. Reipurth, D. Jewitt, and K. Keil), p. 523.
- Watson D. M. et al., 2004 *ApJS*, 154, 1, 391.
- Weidenschilling S. J., 1977 *MNRAS*, 180, 57.
- Weidenschilling S. J. and Cuzzi J. N., 1993 *Protostars and Planets III* (E. H. Levy and J. I. Lunine), p. 1031.
- Weinberger A. J. et al., 1999 *ApJL*, 525, L53.
- Wisniewski J. P. et al., 2008 *ApJ*, 682, 548.
- Woitke P. et al., 2016 *A&A*, 586, A103.
- Woitke P. et al., 2019 *PASP*, 131, 1000, 064301.
- Wolf S. et al., 2002 *A&A*, 385, 365.
- Wolff S. G. et al., 2016 *ApJL*, 818, L15.
- Xiang-Gruess M. and Papaloizou J. C. B., 2013 *MNRAS*, 431, 2, 1320.
- Xie C. et al., 2021 *ApJL*, 906, 2, L9.
- Youdin A. N. and Goodman J., 2005 *ApJ*, 620, 459.
- Yu H. et al., 2021 *ApJL*, 920, 2, L33.
- Zhang K. et al., 2015 *ApJL*, 806, 1, L7.

- Zhang S. and Zhu Z., 2020 *MNRAS*, 493, 2, 2287.  
Zhang S. et al., 2018 *ApJL*, 869, 2, L47.  
Zhou Y. et al., 2014 *ApJL*, 783, 1, L17.  
Zhou Y. et al., 2021 *AJ*, 161, 5, 244.  
Zhu Z., 2015 *ApJ*, 799, 1, 16.  
Zhu Z. et al., 2015 *ApJ*, 813, 2, 88.  
Ziampras A. et al., 2020a *A&A*, 637, A50.  
Ziampras A. et al., 2020b *A&A*, 633, A29.  
Zurlo A. et al., 2020 *A&A*, 633, A119.

## A. Literature references for gallery figures

The data sets shown in Figures 1, 5 and 9, were gathered from the archives and reduced with latest pipeline versions of the respective instruments. Here we list the publications in which the data sets were first described.

**References for Figure 1** From upper left to lower right:

**Disks with rings:** TW Hya (*van Boekel et al. 2017*), RXJ1615-3255 (*Avenhaus et al. 2018*), HD 169142 (*Momose et al. 2015*), Oph IRS 48 (*Follette et al. 2015*).

**Disks with spirals:** GQ Lup (*van Holstein et al. 2021*), EM\* SR 21 (*Muro-Arena et al. 2020*), HD 34700 (*Monnier et al. 2017*), HD 135344B (*Stolker et al. 2016b*).

**Disks with broad shadows:** EX Lup (*Rigliaco et al. 2020*), WRAY 15-788 (*Bohn et al. 2019*, *Wolff et al., in prep.*), HD 143006 (*Benisty et al. 2018*), HD 139614 (*Laws et al. 2020*).

**Disks with narrow shadows:** GG Tau (*Keppler et al. 2020b*), RXJ 1604.3 (*Pinilla et al. 2018*), HD 142527 (*Hunziker et al. 2021*), HD 100453 (*Benisty et al. 2017*).

**Disks with visible backside:** IM Lup (*Avenhaus et al. 2018*), MY Lup (*Avenhaus et al. 2018*), PDS 453 (*Menard et al., in prep.*), HD 34282 (*de Boer et al. 2021*).

**Disks interacting with ambient material:** DO Tau (*Huang et al., subm.*), 2MASS J1615-1921 (*Garufi et al. 2020*), GW Ori (*Kraus et al. 2020*), MWC 758 (*Laws et al. 2020*).

**References for Figure 5** From left to right: HK Lup (*Garufi et al. 2020*), J1609-1908 (*Garufi et al. 2020*), SZ 111 (unpublished), DoAr 44 (*Avenhaus et al. 2018*), RY Lup (*Langlois et al. 2018*)

**References for Figure 9** From upper left to lower right:

**Symmetric/ double-arm disks:** DZ Cha (*Canovas et al. 2018*), V1247 Ori (*Ohta et al. 2016*), MWC 758 (*Benisty et al. 2015*), LkHa 330 (*Uyama et al. 2018*), EM\* SR 21 (*Muro-Arena et al. 2020*), HD 135344B (*Stolker et al. 2016b*).

**Asymmetric/ multi-arm disks:** CQ Tau (*Uyama et al. 2020*), HD 100546 (*Sissa et al. 2018*), AT Pyx (*Ginski et al. 2021a*), HD 142527 (*Hunziker et al. 2021*), RY Lup (*Langlois et al. 2018*), HD 34282 (*de Boer et al. 2021*).

**Flocculent spirals:** SU Aur (*Ginski et al. 2021b*), GG Tau (*Keppler et al. 2020b*), HD 34700 (*Monnier et al. 2017*).

**Interaction with environment:** WW Cha (*Garufi et al. 2020*), DR Tau (*Mesa et al. 2022*), AB Aur (*Boccaletti et al. 2021*).

**Disks with outer companions:** HD 100453 (*Benisty et al. 2017*), GQ Lup (*van Holstein et al. 2021*), UX Tau (*Ménard et al. 2020*)